MDPI

Review

Current Progress of Efficient Active Layers for Organic, Chalcogenide and Perovskite-Based Solar Cells: A Perspective

Francisca Werlinger [1,2], Camilo Segura [1], Javier Martínez [1], Igor Osorio-Roman [1], Danilo Jara [3], Seog Joon Yoon [4] and Andrés Fabián Gualdrón-Reyes [1,*]

[1] Facultad de Ciencias, Instituto de Ciencias Químicas, Isla Teja, Universidad Austral de Chile, Valdivia 5090000, Chile; francisca.werlinger@uach.cl (F.W.); camilo.segura@uach.cl (C.S.); javier.martinez@uach.cl (J.M.); igor.osorio@uach.cl (I.O.-R.)

[2] Facultad de Ciencias Químicas y Farmacéuticas, Departamento de Química Orgánica y Fisicoquímica, Universidad de Chile, Santiago 8380492, Chile

[3] Facultad de Ingenieria y Ciencias, Universidad Adolfo Ibáñez, Av. Padre Hurtado 750, Viña del Mar 2580335, Chile; danilo.jara.q@uai.cl

[4] Department of Chemistry, College of Natural Science, Yeungnam University, Gyeongsan 38541, Republic of Korea; yoon@yu.ac.kr

* Correspondence: andres.gualdron@uach.cl

Abstract: Photovoltaics has become one of the emerging alternatives to progressively supply/replace conventional energy sources, considering the potential exploitation of solar energy. Depending on the nature of the light harvester to influence on its light-absorption capability and the facility to produce electricity, different generations of solar devices have been fabricated. Early studies of organic molecules (dye sensitizers) with good absorption coefficients, going through metal chalcogenides and, lastly, the timely emergence of halide perovskites, have promoted the development of novel and low-cost solar cells with promising photoconversion efficiency (PCE), close to the well-established Si-based devices. However, main drawbacks such as the degradation/photocorrosion of the active layer, the existence of intrinsic defect sites, and the inherent toxicity of the material due to the presence of some harmful elements have blocked the future commercialization of the above kind of solar cells. In this review, we highlight the current progress in achieving efficient photomaterials for organic, chalcogenides and halide perovskites-based solar cells with the purpose of achieving high PCE values, some of which are breakthroughs in this research topic, and the diverse approaches used to extend the stability of the active layer and improve the performance of the solar devices.

Keywords: light harvesting; organic molecules; metal chalcogenides; metal halide perovskites; active layer

1. Introduction

Photovoltaics (PVs) is one of the most important topics in the development of prominent strategies for finding sustainable energies, with sunlight being an unlimited energy source [1]. This factor has been pivotal considering that both the high energy demand around the world and the subsequent replacement of traditional energy sources such as fossil fuels, coke, and natural gas, among others, have been promoted to mitigate the growing environmental contamination and global warming [2,3]. To guarantee a maximum capability of light absorption, the main component of solar devices is based on semiconductor materials, which collect the sunlight to produce free electrons (sunlight-to-current transformation), which are transported through the fabricated cell [4,5]. In order to optimize the absorption of sunlight, various light trapping techniques, including texturing [6], anti-reflective coatings [7,8] and plasmonic effects [9], can be employed. These methodologies are implemented to enhance the capture of light within the active layer of a solar cell. Furthermore, it is relevant to mention that to certify the performance of

the fabricated devices, some operational parameters are established, such as the simulated sunlight intensity, which should contain the AM 1.5 G filter, and the direction of the voltage scanning (forward/reverse) during the photovoltaic measurements. For this contribution, we show the maximum photoconversion efficiency developed by the different solar cells, independent of the direction of voltage scanning, considering that the reported performance is established for optimized devices (ideally similar efficiency in forward and reverse measurements).

For decades, silicon (Si)-based solar cells have dominated the photovoltaics market because these devices can reach photoconversion efficiencies (PCEs) of more than 20%, the photomaterial is non-toxic, providing good photoconductivity properties, resistance to corrosion, and high light intensities and temperatures [4,5,10]. However, even though Si-based solar cells can be obtained by using different Si active layers (monocrystalline, polycrystalline, nanostructured and amorphous Si films), the material preparation and processing are high energy demanding processes to melt the Si source, which increases the fabrication cost for Si-based solar cells [11]. Hence, the final costs of the device production and installation increases, which is a huge challenge in solar technologies. With the purpose of offering a step forward in the fabrication of lower-cost solar cells with promising PCE, another kind of semiconductor has been introduced, as in the case of II-VI type CdTe thin films [12,13]. This type of chalcogenide can be directly deposited as a polycrystalline film through low-cost techniques including close vapor transport [14], laser ablation [15], sputtering [16] and electrodeposition [17]. CdTe thin films have also been prepared by using chalcogenide nanoparticles dispersed in organic or aqueous solutions and deposited by dip-coating/spin-coating techniques, followed by an annealing process [18–20].

On the other hand, CdTe shows an optimal band gap ~1.42 eV (indicating a suitable light harvesting feature in a wide range of the UV-vis-NIR spectrum), direct band transitions, and a high absorption coefficient ~10^4 cm^{-1} [21]. This feature is adequate for absorbing ~90% of incident illumination for 1 μm thickness CdTe film. Additionally, this chalcogenide can be produced with n- or p-type semiconductivity, making it ideal for establishing heterojunctions for carrier transfer. Nevertheless, some disadvantages, such as a high resistance to carrier transport and fast surface recombination, hinder electron mobility through the solar devices, decreasing their operational performance [22]. In this way, reasonable approaches such as the preparation of chalcogenide-based heterostructures, for instance, CdS/CdTe ones, are known to enhance carrier injection and transfer into the solar cell, which increases the net PCE [23,24]. Unfortunately, the recent PCE is far from the established record of solid-state solar cells, some of them based on tandem perovskite-Si devices (whose main properties are highlighted below), and it is deductible that a wide understanding of the required components of the solar cells and the quality of the active layer should be pivotal in order to increase the PV efficiency.

The first step to maximizing the sunlight harvesting in low-cost PV devices was introduced by Grätzel in 1991 [25], to fabricate dye-sensitized solar cells (DSSCs) by using natural/synthetic organic materials. These molecules favored carrier generation and transport, obtaining an initial PCE of 10%. As shown in Figure 1 [26], DSSCs are based on the deposition of ruthenium (II) polypyridyl complex monolayers on TiO$_2$ films acting as working electrodes (photoanodes). Meanwhile, platinum-transparent glass is used as a counter electrode (also called a cathode), being coupled with the active layer to achieve the expected device. The operational performance of the DSSCs to produce electricity depends on the efficiency of exciton formation. In this scenario, the photogenerated electrons coming from the highest occupied molecular orbital (HOMO) of the organic complex (hereafter named sensitizer) are accumulated in the lowest unoccupied molecular orbital (LUMO), and then transferred to the conduction band (CB) of the TiO$_2$ layer. Then, these carriers are transported to the external circuit of the PV cell to reach the cathode, generating photocurrent. The electron depletion in the HOMO of the dye is filled by electrons from the electrolyte, which is composed of a redox system based on the I$^-$/I$_3^-$ pair. Lastly, iodide is regenerated by reducing the triiodide species through electrons collected by the cathode,

closing the circuit where the current is produced. This contribution opened the door to new organic photomaterials based on dyes, polymers, and small molecules with suitable electronic properties, giving the possibility to fabricate organic solar cells [27–29]. Although the selective contacts (electron and hole transporter layers, ETL and HTL, respectively) impact carrier generation and transport into the PV device, organic molecules exhibit limited light harvesting in a wide range of the energy spectrum and restrained exciton diffusion [30]. These features favor a decrease in carrier density to be transported into the solar cells, hampering their operational performance.
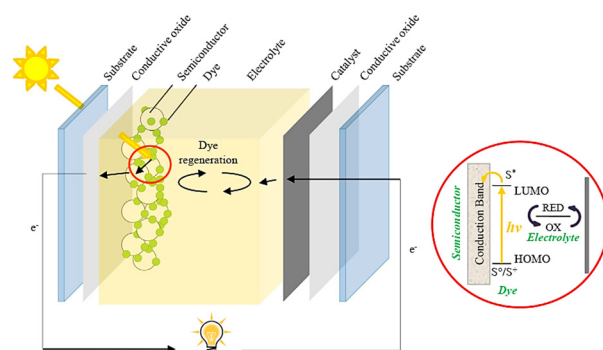

Figure 1. Schematic illustration of a typical dye–sensitized solar cell. The device describes carrier transport from the dye (after carrier excitation from the ground state, S^o/S^+ to the excited state, S^*) to the semiconductor. Redox electrolyte renews the carriers to the sensitizer for carrying out the photovoltaic process. Reproduced with permission [26]. Copyright 2014. Elsevier.

Attending to the above device configuration from the DSSCs, organic molecules have been replaced by inorganic hybrid sensitizers, as in the case of Cd-free chalcogenides (in form of quantum dots, QDs); see Figure 2a [31–34] and then halide perovskite (HPs) type active layers (in the form of bulk); see Figure 2b [35,36], with fascinating features such as high absorption coefficient, long carrier diffusion length, and modulable optical properties depending on the photomaterial size and composition. These advantages allow for the extension of the the light harvesting even to the IR range of the energy spectrum, improving the capability of the sensitizer to generate the photocarriers required to favor a high PCE [37]. In this context, the band gap and relative band positions of the QDs and bulk perovskites can be modified to match the ETL and HTL and thereby facilitate the carrier injection to the selective contacts to generate the expected photoresponse [38,39]. Chalcogenide QDs have reached a maximum PCE of 14.4% [40], while HP bulk films have achieved PCE close to 26% [41,42], overpassing the actual performance of the Si- and CdTe-based technologies. Interestingly, most of the abovementioned features of both kind of active layers are also useful for another kind of research application, such as the fabrication of photodetectors with high responsivity and specific detectivity [43–51].

The combination of HPs-based solar cells (PSCs) and Si-solar devices has promoted the development of tandem solar cells, with PCE values of 33.2% [52]. The transparency and thickness control of the active layers and the band gap tuning have been considered to be promising devices for future commercialization. Despite the light-to-current transformation being eventually improved in current prototypes of solar cells, the use of inorganic materials is found to be restrained due to their ionic nature, which produces photocorrosion in chalcogenides [53] and the formation of non-photoactive crystalline phases in HPs, as in the case of iodide-HPs.
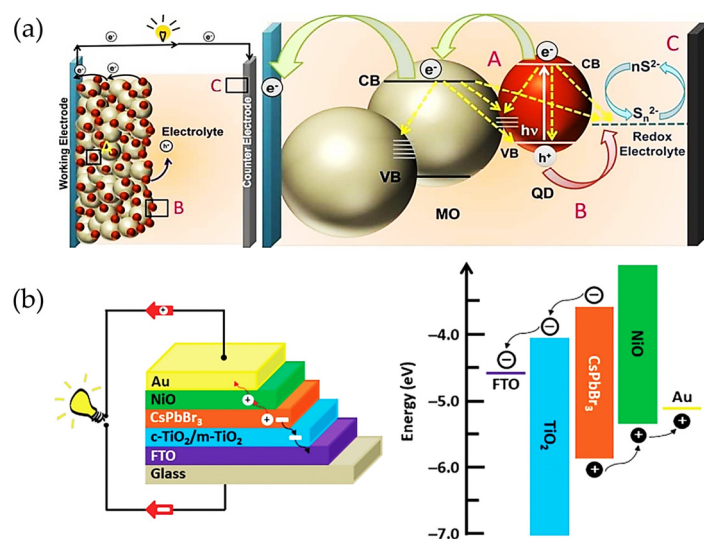
Figure 2. (**a**) Schematic representation of the working principle of a quantum dot-sensitized solar cell (QDSSC). A, B and C describe the possible ways of carrier transport: A—QDs-semiconductor, B—redox electrolyte—QDs, C—counter electrode to redox electrolyte. Yellow arrows indicate the possible carrier recombination pathways in each component of the QDSSC; reproduced with permission [34]. Copyright 2018. American Chemical Society. (**b**) Schematic of a conventional architecture of a perovskite solar cell (PSC) and the corresponding relative energy positions of the components of the solar device; reproduced with permission [36]. Copyright 2019. John Wiley & Sons, Inc.

As shown above, reports have widely discussed the fundamentals of the photovoltaic effect in solar cells, which have been adopted to describe the way that the active layers, or sensitizers, capture the sunlight to produce electricity through the formation of photo-carriers, which are separated and transported through the devices. This fact has led some researchers to believe that the emergence of the following generation of solar cells offers more advantages than the previous one, but it has not been deeply explained from the point of view of individual components how the fabrication of innovative solar devices can be more efficient and exhibit enhanced long-term stability. More specifically, few reports have consolidated the advantages/disadvantages of using different types of materials as active layers, where the photovoltaic effect starts, and some explanation about how the integration of these sensitizers into a coupled solar system can magnify the net performance of a solar cell to be competitive with the actual commercialized Si-based ones has not been widely highlighted.

Overall, in this review, we highlight the current progress in the preparation of novel active layer materials to fabricate more efficient organic, chalcogenide, and perovskite solar cells, obtaining valuable information about their operational stability, and including the use of less toxic species to produce more profitable solar technologies in the near future. Unlike actual reports where a general description of the characteristics of each component of the solar device (electron/hole transporting and active layers) is provided, we mainly focused on the light absorption and carrier separation/transport capabilities of suitable active layers to fabricate efficient solar cells from diverse device generations. Some critical disadvantages, such as band structure mismatch, low absorption coefficient, presence of defect sites for carrier recombination, and degradation of the photoactive crystalline phase, are mentioned throughout the manuscript. Nevertheless, some benefits, such as a tunable band gap depending on the nature of the photomaterial and a versatile surface chemistry, are analyzed to understand the actual challenges of using several types of active layers, offering the opportunity to establish an adequate one for future commercialization purposes. In this context, a perspective on prominent and suitable photomaterials acting as active layers in solar devices is also addressed.

The review is divided into three main topics: organic solar cells, chalcogenide solar cells, and halide perovskite-based solar cells, and the application of novel photomaterials as active layers in solar devices is thoroughly addressed. This order of showing the main features of each active layer was chosen, considering the level of actual interest in the development of this type of photomaterial. Although the current interest in some of them has decreased, we consider these materials have opened the door to understanding the photovoltaic process in a solar cell configuration and what the most relevant properties of the material itself are to make it suitable for photovoltaics.

2. Progress in the Development of Active Layers for Efficient PV Devices

2.1. Organic Solar Cells

Organic solar cells (OSCs) have recently attracted attention worldwide since they are one of the most promising energy sources due to their distinctive advantages, such as light-weight mechanical flexibility, being colorful, translucent, nontoxic and being solution-processable for huge area fabrication [54–58]. Over the last three decades, the area of OSCs has made impressive progress in efficiency, which probably makes them a competitive alternative to inorganic solar cells in the near future. In this review, we are going to classify OSCs into three different groups based on their structure: binary, ternary, or tandem OSCs and dye-sensitized solar cells (DSCs).

2.1.1. Binary, Ternary, and Tandem Organic Solar Cells

The first manufacture of organic photovoltaic solar cells was based on single organic films inserted between two metal electrodes of different work functions [59,60]. Initially, organic materials with p- and n-type conductivities are deposited on a transparent electrode, and then the metal electrode is placed over them. The operation of OSCs consists of the fact that sunlight is absorbed by organic layers, and produced excitons are dissociated to electrons and holes at the interface amongst p- and n-type organic layers. Finally, holes and electrons are diffused at the electrodes, generating electricity [59–61]. The PCEs reported by these devices were really poor (around 0.01%), although they reached a significant 0.7% with the incorporation of merocyanine dyes [62,63]. The next evolution in this area was performed by introducing the heterojunction concept, in which two organic films with special electron- or hole-transporting properties were sandwiched between the electrodes. Tang and coworkers [64] manufactured the first organic photovoltaic device based on planar heterojunction (PHJ) of two organic materials (phthalocyanine and perylene derivatives), one carrier donor, and one carrier acceptor, which were used to distribute the excitons. These organic layers were sandwiched between a transparent conducting oxide and a semitransparent metal electrode, affording effective charge extraction. Although there were very few donor/acceptor interfaces, this device was quite limited. This solar cell afforded around 1% of PEC, which was the best result obtained for almost 10 years.

On the other hand, the development of conjugated polymers grew enormously in the early 1990s, although their incorporation as single-layer devices was not initially successful since the values of PCEs obtained by this type of material were less than 0.1% [65,66]. Nevertheless, the discovery of photoinduced electronic transference between optically excited conjugated polymers and the fullerene molecule (C_{60}) [67,68], along with the elevated photoconductivities shown by the addition of C_{60} to the conjugated polymers [69], allowed the fabrication of devices based on polymer-fullerene bilayer heterojunction [70,71] or bulk heterojunction (BHJ) [72–74]. This advance significantly increased the values of PCEs of the corresponding devices for almost two decades (Table 1) [75–82]. The photoinduced electron mobility favorably happens in the polymer-fullerene system when the electron in the excited state of the polymer is transferred to the fullerene, which is quite more electronegative since the electron is injected from a p-type hole belonging to the conducting polymer, donor (D), to the n-type electron from the conducting C_{60} molecule, acceptor (A) [83]. This occurs because fullerene derivatives present a fully conjugated structure, which gives them powerful electron-accepting and isotropic electron-transport abilities and favors

electron delocalization at the D:A interfaces [84,85]. Some time ago, it was believed that fullerene materials such as $PC_{61}BM$ ([6,6]-phenyl-C_{61}-butyric acid methyl ester) [86], F1 ([6,6]-phenyl-C_{61}-propionic acid methyl ester) [87], and F [88] (Figure 3) were a basic component for efficient operation of OSCs. However, this scenario has recently changed with the appearance of non-fullerene acceptors (NFA) such as ITIC (3,9-bis(2-methylene-(3-(1,1-dicyanomethylene)-indanone)-5,5,11,11-tetrakis(4-hexylphenyl)-ditheno [2,3-d:2′,3′-d′]-s-indaceno [1,2-b:5,6-b′]-dithiophene) [89], ITIC-Th1 (3,9-bis(2-methylene-(5&6-fluoro-(3-(1,1-dicyanomethylene)-indanone)-5,5,11,11-tetrakis(4-hexylthienyl)-dithieno [2,3-d:2′,3′-d′]-s-indaceno [1,2-b:5,6-b′]-dithiophene) [90], FOIC [91], and Y6 ((2,20-((2Z,20Z)-((12,13-bis(2-ethylhexyl)-3,9-diundecyl-12,13-dihydro-[1,2,5]thiadiazolo [3,4-e]thieno [2,″30′:4′,50]thieno [20,30:4,5]pyrolo [3,2-g]thieno [20,30:4,5]thieno [3,2-b]indole-2,10-diyl)bis(methanylylidene)) bis(5,6-difluoro-3-oxo-2,3-dihydro-1H-indene-2,1-diylidene))dimalononitrile)) [92] (Figure 3), which have increased notably the values of PCEs obtained [84,93]. The performance of the NFA-based OSCs is closely related to the morphology of the functional layers and the material processing, although in some cases the change in the stratification of the donor and acceptor in the BHJ [94–96] and the chemical stability at the BHJ/contact interfaces [97] have also played a decisive role in increasing the PCE values in these devices. The fast development of OSCs based on NFA has caused these devices have crossed the PCE barrier of 19% over the last years; see Table 1 [98–105]. Nevertheless, the broad range of donor molecules previously used for fullerene OSCs provided a splendid library for direct use in NFA OSCs. From the device perspective, excitons in NFA OSCs can be effectively separated by negligible driving energies, which contributes to increasing their PCEs. Consequently, this type of devices regularly shows elevated photocurrent and low voltage losses simultaneously; nonetheless, fullerene-based OSCs present problems under low driving energies frequently [99].

The PCE is calculated in OSCs by multiplying the values of open-circuit voltage (V_{oc}), short-circuit current density (J_{sc}), and a fill factor (FF). The value of V_{oc} essentially depends on the level of the donor's HOMO and acceptor's LUMO; the J_{sc} value is correlated to the absorption and surface of the active layer; and the value of FF is related to the charge carrier mobility. Table 1 includes the highest PCE values recently reported for binary OSCs [106].

Table 1. Photovoltaic performances of the recently reported binary OSCs.

Binary OSCs	J_{sc} (mA/cm^2)	V_{oc} (V)	FF	PCE (%)	Stability	Ref.
PF2:PC$_{71}$BM	15.00	0.75	0.744	8.40	72% of initial performance, 3.33 h, air	[75]
DCPY2	22.24	0.90	0.650	13.02	90% of initial performance, 700 h, 85 °C, air	[77]
PM6:L8-BO	26.68	0.88	0.805	19.02	70% of initial performance, 130 h, air	[107]
BTI-2T-CNA:IDIC	12.90	0.89	0.581	6.70	-	[108]
BTP-eC9:BTP-ICBCF$_3$	27.40	0.85	0.778	18.20	-	[109]
PBDB-TF:HF-PCIC	17.24	0.89	0.710	10.90	90% of initial performance, 700 h, 130 °C, air	[110]
BTP-O-S	24.40	0.90	0.782	17.10	-	[111]
PM6:L8-BO	25.81	0.90	0.801	18.69	86% of initial performance, 500 h, air	[112]
PM6:BTP-eC9	27.88	0.86	0.804	19.31	70% of initial performance, 1000 h, air	[98]
D18:L8-BO	26.70	0.89	0.800	19.00	74% of initial performance, 200 h, 80 °C, air	[101]
PEDOT:PSS	25.70	0.87	0.791	18.03	88% of initial performance, 1200 h, air	[113]

In general, the working mechanism in bulky heterojunction OSC devices occurs as follows: (a) photons are absorbed and excitons are generated; (b) excitons are diffused to D/A interfaces; (c) excitons are dissociated in holes and electrons at D/A interfaces, which are transported to the electrodes; see Figure 4 [114,115]. The BHJ system was first introduced by combining two polymers with acceptor and donor properties in solution [116], which solved the problems shown by PHJ systems. One of the best OSCs reported to date is based on this type of structure due to its numerous advantages, such as semi-transparency, light weight, and high mechanical flexibility [117–120]. However, BHJ structure has some drawbacks, such as their morphology; it is difficult to control them since an inadequate morphology could promote a fast charge recombination, affecting electron diffusion at the interface between donor and acceptor moieties, which also influences the recombination

between holes and electrons [120]. These disadvantages could influence the industrial development of OSCs based on BHJ because controlling the nanostructure of the donor and acceptor is a complicated task. Accordingly, the performance of OSCs has been significantly improved by efforts to design new donor and acceptor materials.
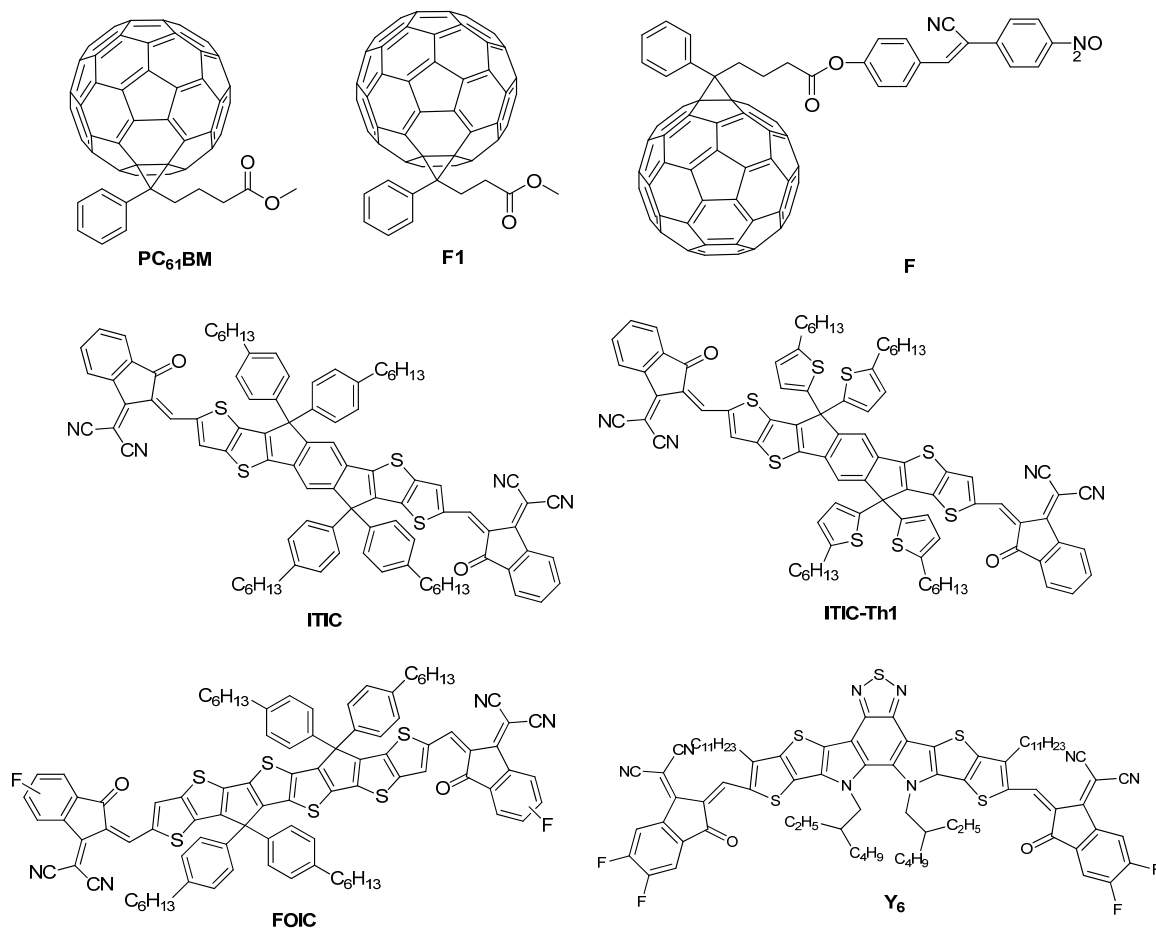

Figure 3. Chemical structure of fullerene derivatives such as PC$_{61}$BM [86], F1 [87], and F [88] and NFA derivatives such as ITIC [89], ITIC-Th1 [90], FOIC [91], and Y6 [92] employed in OSCs.
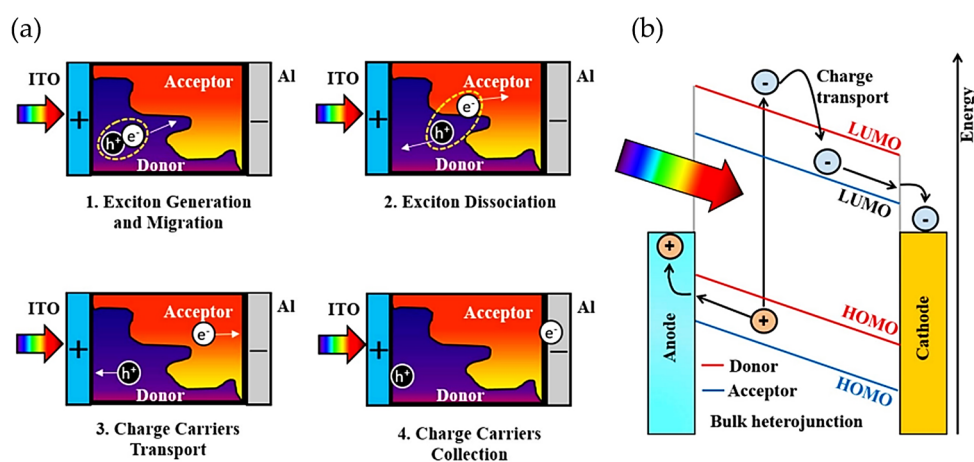

Figure 4. (**a**) Steps involved in energy production upon illumination (From exciton generation until charge carrier collection). (**b**) Band diagram of the photocurrent generation mechanism in a BHJ solar cell. Reproduced with permission [115]. Copyright 2018. Elsevier.

The main limitation of OSCs is that organic materials show an absorption width of only about 0.5 eV, so the binary single-junction can only take advantage of a small part of the solar radiation, hindering the improvement in device efficiency [84,121]. For these reasons, the introduction of a ternary blend based on a dye, nanoparticle, polymer, or small molecule into the device could solve the aforementioned problems [100], and ternary OSCs have recently focused the attention of the scientific community because these devices could afford great PCE values (Table 2). Basically, ternary OSCs are formed by three units, two acceptor moieties, and one donor (or two donor moieties and one acceptor) (Figure 5) [122].
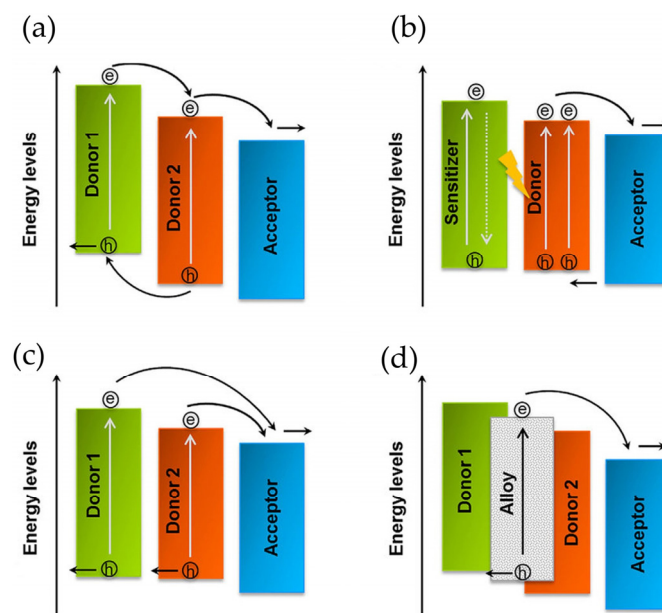

Figure 5. Schematic, working principles in ternary OSCs. (**a**) Mechanism of charge transportation (additional donor functions for charge transport). (**b**) Mechanism of energy transfer (from photo-excited sensitizer to host donor). (**c**) The parallel like mechanism (formation of independent hole transport network from the additional donor). (**d**) The alloy model (coupling of new charge-transfer state by host donor). The arrows show the proposed path for charge carrier and charge transportation. Reproduced with permission [122]. Copyright 2018. John Wiley and Sons, Inc.

Firstly, the third component has been used as a sensitizer, assisting in extending the maximum absorption of the acceptor and the donor based on the 1-(3-methoxycarbonyl) propyl-1-phenyl [6,6] methano-fullerene (PCBM) matrix. In addition, considering the first reports about ternary OSCs, scientists have employed a huge variety of organic entities as third components, which act as an efficient charge transport pathway, boosting charge transport and exciton dissociation for OSC devices [100]. These ternary devices, which are mainly based on polymer/small molecule/PCBM, polymer/PCBM/non-fullerene, and polymer/ICBA/PCBM (ICBA, indene-C_{60} bis-adduct), reported PCE values above 10% (Figure 6) [123–125]. Ternary OSCs can be classified in four categories according to their function: charge transfer, energy transfer, parallel like, and alloy models. It is important to mention that the most efficient ternary OSCs operate under an alloy-like model since the gradual changes in V_{oc} depend on the third element.

Table 2. Photovoltaic performances of the recently reported ternary OSCs.

Ternary OSCs	J_{sc} (mA/cm^2)	V_{oc} (V)	FF (%)	PCE (%)	Stability	Ref.
TO:PEDOT:PSS (S11)	17.62	0.95	0.701	11.78	70% of initial performance, 1008 h, 85 °C, air	[126]
PM6:PY-V-γ:PFBO-C12	25.80	0.91	0.770	18.00	80% of initial performance 1000 h, air	[127]
PEDOT:PSS:LiF	25.60	0.86	0.742	16.70	55% of initial performance, 360 h, air	[128]
PM6:Y6:7.5%FPDI-2PDI	27.47	0.85	0.772	18.00	55% of initial performance, 30 h, air	[129]
PM6:M-Cl:O-Cl	27.40	0.87	0.762	18.10	-	[130]
D18:Y6:SN-O	26.80	0.88	0.781	18.30	-	[131]
PBQx-TF:eC9-2Cl:F-BTA3	26.70	0.88	0.809	19.00	-	[105]
PBDB-T-2F:Y6:SF(BR)$_4$	29.31	0.89	0.800	20.87	-	[132]
PBQx-TCl:PBDB-TF:eC9-2Cl	27.15	0.89	0.811	19.51	-	[133]

Since single organic materials have the ability to absorb at different wavelength regions between the blue and the infrared regions, "tandem" architectures have been designed to accomplish higher performances in OSCs with better use of near-infrared (NIR) solar energy [134]. Tandem OSCs are formed by two sub-cells, a front and back sides, both made of organic materials. For certain types of OSCs with a specific bandgap and absorption region, the balance between the loss of photon energy by thermalization and spectrum unitization is limited [135]. However, in tandem OSCs, the absorption spectrum can be extended by using a wide bandgap sub-cell to employ high-energy photons and another narrow bandgap sub-cell for employing low energy photons [136]. In this context, the V_{oc} value presented by tandem OSCs is normally higher than that of binary or ternary OSCs because it is the sum of those of the two sub-cells, whereas the J_{sc} value usually derives from the sub-cell with relatively lower J_{sc}; hence, the PCE in tandem OSCs depends directly to the balance between V_{oc} and J_{sc} for each sub-cell, which is decisive for the high efficiency of the device [134,137]. At the current stage, the PCE values of tandem OSCs are very similar to those presented by binary or ternary OSCs, as seen in Table 3. The main difficulty for the development of tandem OSCs is related to their design since the current of each sub-cell has to be matched, so the total current of the device is limited by the lowest current generating sub-cell [85]. Another limitation of this device is related to the low efficiency presented by organic materials for narrow band gap sub-cells, which would allow the use of the NIR region of the solar spectrum.

Table 3. Photovoltaic performances of the recently reported tandem OSCs.

Tandem OSCs (Front/Back Cell)	J_{sc} (mA/cm^2)	V_{oc} (V)	FF	PCE (%)	Stability	Ref.
PTB7-Th:BTPV-4F/PTB7-Th:BTPV-4F:PC$_{71}$BM	14.50	1.65	0.690	16.40	-	[120]
PBDT [2F]T:PC$_{71}$BM/PCE10:PC$_{61}$BM	7.10	1.61	0.705	8.30	-	[138]
PBDB-T:F-M/PTB7-Th:O6T-4F:PC$_{71}$BM	14.35	1.64	0.737	17.36	96% of initial performance, 3984 h, air	[139]
PM7:TfIF-4Cl/PTB7-Th:COi8DFIC:PC71BM	14.59	1.64	0.780	18.71	95% of initial performance 500 h, air	[140]
PM6:GS-ISO/PM6:BTP-eC9	13.14	2.01	0.768	20.27	87% of initial performance, 450 h, air	[141]

2.1.2. Dye-Sensitized Solar Cells

Conceptually similar to the BHJ, there is another broad research field based on DSSCs. The early development of these devices was performed by the Grätzel research group [25,142–144]. As discussed previously, DSSCs have greatly focused the attention of the scientific community over the last few years due to their promising performance and low fabrication cost [145,146]. It is important to highlight that water-based electrolytes DSSCs are being developed owing to their interesting advantages such as reduced volatility, non-flammability, and environmental compatibility, affording a PCE value over 7% [147]. Additionally, DSSCs are able to be produced on a large scale and present a commercial application for self-powering systems and portable electronics [148,149]. On the other hand,

specifically DSSCs prepared with copper-complex-based redox mediator have shown great progress in obtaining PCE values close to 13%, since their V_{oc} can achieve values over 1.0 V [148,149], lower compared to the values observed by high performance tandem OSCs; see Table 3. However, these devices exhibit low J_{sc} values, considerably reducing their PCE performance. Probably, the principal disadvantage of DSSCs compared with other OSCs is related to the relatively low PCE values reported for these devices; it is difficult to find DSSCs with PCE values over 14%. On the contrary, the most important advantage of DSSCs is their ability to exhibit outstanding stability, maintaining high percentages of their initial PCE after long periods of time.

2.1.3. Comparison of J–V Curves and Normalized PCE vs. Time for Different Types of Organic Solar Cells

Binary, ternary, and tandem OSCs or DSSCs are devices with different characteristics that are determined by their values of V_{oc}, fill factor (FF) and J_{sc}. These variables are defined by the current density and voltage (J–V curves) properties of the solar cells [99]. These parameters are closely related to the photoactive materials (acceptor and donor materials). Thus, the number of free carriers collected at the electrodes at zero applied potential ($V_{oc} = 0$) is what determines the value of J_{sc}. The energy difference amongst the HOMO and LUMO orbitals of the acceptor and donor materials influences the highest voltage that a solar cell could extract for an external circuit, ascribed to the value of V_{oc}. For example, in PM1:BTP-eC9 systems, device efficiency improved from 17.86% to 19.10% with TCB processing. It is important to comment that the TCB-ISM device exhibits the highest PCE value (19.31%) reported to date for a binary OSCs; see Figure 6a [98]. Additionally, the ternary blend PBQx-TCl:PBDB-TF:eC9-2Cl displays a maximum PCE of 19.51%, a V_{oc} of 0.886 V, a J_{sc} of 27.15 mA cm^{-2}, and an FF of 81.14%; see Figure 6b [133]. The tandem OSC based on ICLs of e-TiOx/PEDOT:PSS system achieved a V_{oc} value over 2.0 V, which is considerably higher than the values of V_{oc} showed by binary or ternary OSCs, affording a PCE value of 20.27%; see Figure 6c [141]. It is important to highlight that DSSCs with ZS4 performed a J_{sc} of 16.3 mA cm^{-2}, as well as a great V_{oc} value of 1.05 V, accomplishing an impressive PCE of 13.2% under AM1.5G sunlight. This efficiency is the highest one reported for copper-electrolyte-based DSSCs with a single sensitizer; see Figure 6d [145].

Having discussed the typical performance of the binary, ternary, tandem OSCs and DSSCs, it is pivotal to focus on studying their stability over time. To address this point, we highlight the stability presented by some of the previously mentioned devices; see Figure 7. The operational stability of binary PM6:BTP-eC9-based OSCs showed a stronger initial decay in PCE, dropping a 17% efficiency during the first 75 h when DIO (1,8-diiodooctane) was used as an additive, while the efficiency of the TCB (1,3,5-trichlorobenzene) treated device only decreased by 7% at the same time. After 1000-h simulated 1-sun illumination stress test at maximum power point (MPP), the TCB-treated device maintained a 78% of initial efficiency; see Figure 7a [98]. The ternary PBDB-TF/HC-PCIC/PC$_{71}$BM experienced an intense drop in efficiency (15%) after only 1 h. However, its efficiency remained constant during the following 10 h; see Figure 7b [110]. Tandem cells dropped sharply in the first 10 h and became stable within 456 h under continuous 1 sun illumination; see Figure 7c [141]. Finally, DSSC fabricated with ZS4 exhibited excellent stability, keeping 95% of their initial PCE under continuous light soaking at 45 °C for 1000 h; see Figure 7d [145]. In general, binary and ternary OSCs reported high PCE values (~20%); however, most of these devices are not very stable over time since their efficiency decreases significantly after a few hours. In contrast, although the PCE values shown by DSCs are moderate (~14%) compared to binary or ternary OSCs, the most important benefit of these types of devices is possibly their capability to display outstanding stability, maintaining elevated percentages of their initial PCE after long periods of time.
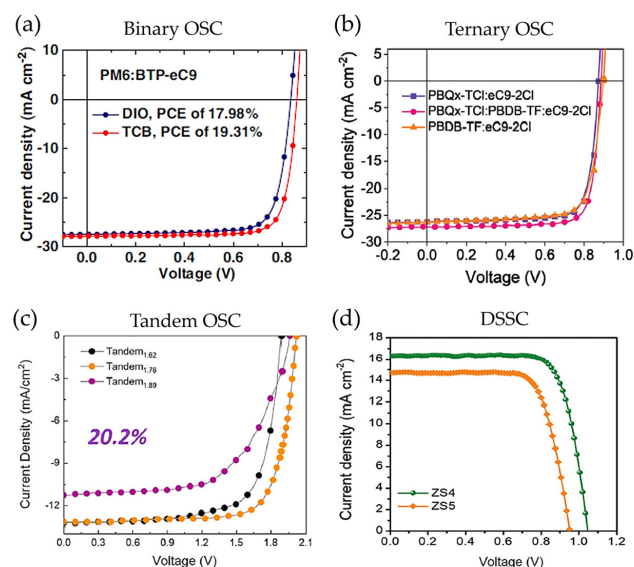
Figure 6. (**a**) J–V curves for the DIO processed and TCB processed OSCs based on PM6:BTP-eC9. Reproduced under the terms of the CC-BY license [98]. Copyright 2023. The Authors. Published by Springer Nature. (**b**) J–V curves of the OPV cells based on the PBQx-TCl:eC9-2Cl, PBDB-TF:eC9-2Cl, and PBQx-TCl:PBDB-TF:eC9-2Cl (0.5:0.5:1.2) systems. Reproduced with permission [133]. Copyright 2023. John Wiley and Sons. (**c**) The J–V curves of tandem OSCs based on ICLs of e-TiOx/PEDOT:PSS under AM 1.5G, 100 mW/cm^2. Reproduced with permission [141]. Copyright 2021. Elsevier Inc. (**d**) J–V curves of the DSCs with ZS4 and ZS5 measured under AM1.5G illumination. Reproduced with permission [145]. Copyright 2023. John Wiley and Sons.
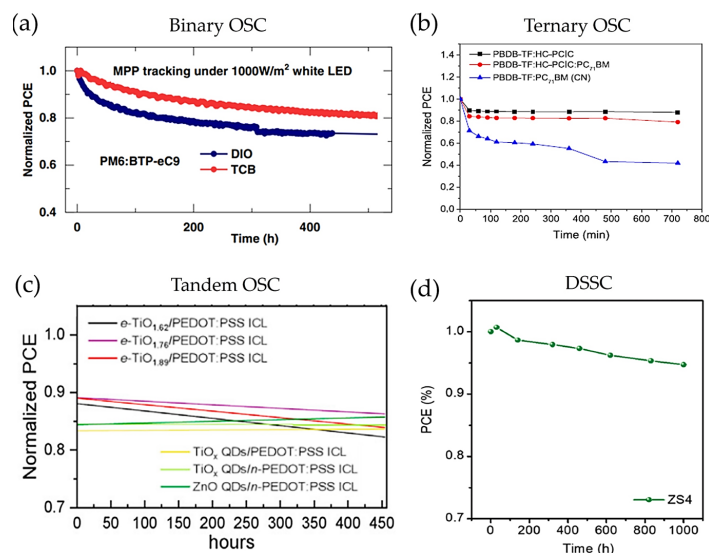

Figure 7. (**a**) Light stability tests for PM6:BTP-eC9-based OSCs with different treatments, all OSCs were encapsulated and stored under continuous illumination equivalent to 1 sun in air. Reproduced under the terms of the CC-BY license [98]. Copyright 2023. The Authors. Springer Nature. (**b**) PCEs for the devices based on PBDB-TF:HC-PCIC, PBDB-TF:HC-PCIC:PC$_{71}$BM, and PBDB-TF:PC$_{71}$BM (CN) blended films after thermal treatment at 130 °C for various times. Reproduced with permission [110]. Copyright © 2018. American Chemical Society. (**c**) The cell degradation diagram of the tandem cells with various ICLs. Reproduced with permission [141]. Copyright 2021. Elsevier. (**d**) Evolution of PCE of DSCs based on dye ZS4 measured under standard AM1.5G sunlight during continuous light soaking at 45 °C for 1000 h. Reproduced with permission [145]. Copyright 2023. John Wiley and Sons.

2.2. Chalcogenide Solar Cells

Chalcogenide solar cells are a class of thin-film solar cells that utilize semiconductor materials from the chalcogenide group (e.g., sulfur, selenium, tellurium) to absorb the solar radiation, produce photocarriers, and thereby generate electricity. These solar cells have the advantage of being cost-effective, with good conversion efficiencies. They typically consist of a substrate, transparent conductive oxide layer, p-type and n-type chalcogenide layers, and an intrinsic layer. Here, we will explain some characteristics of binary, ternary, and quaternary chalcogenides usually employed for the fabrication of solar devices.

2.2.1. Binary, Ternary, and Quaternary Chalcogenides

Binary chalcogenide solar cells use semiconductor materials composed of two elements, one from the chalcogenide group, such as sulfur (S), selenium (Se), or tellurium (Te) and a metal. These materials are abundant and relatively low-cost, making them attractive for solar cell applications. The structure of binary chalcogenide solar cells typically consists of a substrate, a transparent conductive oxide layer (TCO), a p-type chalcogenide layer, an intrinsic layer, and an n-type chalcogenide layer. The TCO layer allows light to pass through while providing electrical conductivity. The p-type and n-type chalcogenide layers help in creating an electric field and facilitating the movement of charge carriers. When sunlight is absorbed by the chalcogenide layers, electron-hole pairs are created, which are then collected to generate an electric current [150]. Among the main types of binary solar cells are as follows:

Cadmium Telluride (CdTe)

A thin-film of CdTe semiconductor absorbs radiation in the visible part of the spectrum, creating electron-hole pairs. The generated electrons and holes are separated at the junction, resulting in a flow of electric current [150]. One of the examples of efficient CdTe solar devices has been described by Rashid and coworkers [151] where a silicon carbide (3C–SiC)-based buffer layer was introduced into the preparation of CdTe films and subsequently device fabrication. By improving the crystallinity of the active layer and providing an adequate heterojunction of the chalcogenide and the 3C-SiC, a PCE value up to 17.29%; see Figure 8a. Clearly, diverse device optimizations have been incorporated during the fabrication of CdTe solar cells, allowing PCE values up to 23% [106]. Among its advantages are cost-effectiveness due to abundant and low-cost materials and compatibility with large-scale manufacturing. However, its main problem is the use of toxic materials [152]. To improve the stability of these devices and avoid the possible lixiviation of Cd, the incorporation of small amounts of cupper during chalcogenide etching process (chemical etch), can be carried out [153]. In this context, optimized CdTe solar devices can preserve 80% of initial performance for close to 1200 h in air; see Figure 8b.

Cadmium Selenide (CdSe)

These thin-film solar cells operate in the same way as CdTe ones, changing the layer that absorbs the sun's photons for one of CdSe [154].

Lead Sulfide (PbS)

These solar cells are known for their ability to efficiently absorb infrared light. PbS solar cells can be fabricated using low-cost solution-based processes [155]. They have shown promise for applications in low-light conditions. For PbS solar cells, PCEs have reached values up to 13.8% [156].

Meanwhile, ternary and quaternary chalcogenides solar cells are a type of thin-film solar cells that are composed of three or four different elements from groups 11–16 of the periodic table, typically including a combination of metal, chalcogen, and sometimes halide elements [157]. These materials have unique electronic properties, such as their tunable bandgap and high absorption coefficient, that make them promising candidates for use in

solar cells. Some of the principal ternary and quaternary chalcogenides used in solar cell applications are as follows:

Copper-Indium-Gallium Selenide (CIGS)

The CIGS solar cell structure consists of several layers, including a back contact, a p-type CIGS absorber layer, an n-type buffer layer, and a transparent front contact [158]. CIGS solar cells have advantages including high efficiency, low temperature coefficient, and the ability to be manufactured using a variety of techniques [158]. The high efficiency of CIGS solar cells is due to the material's ability to absorb a large fraction of the solar spectrum, including both visible and infrared light [159,160]. Additionally, CIGS solar cells have a low temperature coefficient [161], meaning their efficiency is less sensitive to changes in temperature compared to other types of solar cells [162]. CIGS solar cells have achieved record PCE of up to 23.35% [163]. The main drawbacks that CIGS cells have are the use of toxic materials and the high temperatures that are needed for their manufacture [164]. On the other hand, by taking advantage of the band gap modulation, CIGS can reach PCEs higher than 21.8% [165], which becomes useful for the fabrication of tandem devices; see Figure 8c. Some optimized devices for this type of active layer can keep ~88% of initial efficiency in harsh conditions of H_2O/O_2 for close to 350 h [166]; see Figure 8d.
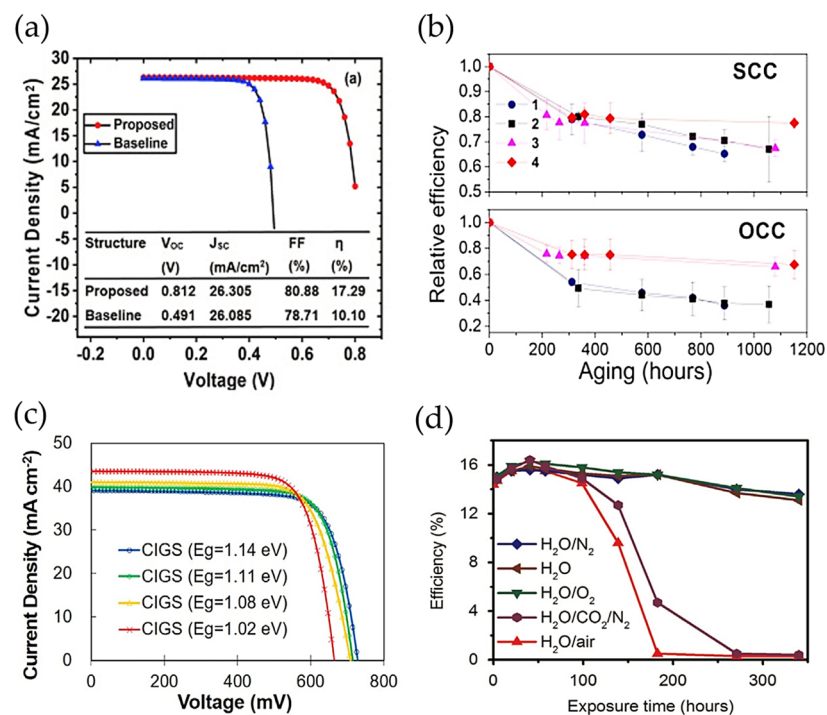

Figure 8. Operational performance and stability of some chalcogenide solar cells. (**a**) J–V curve of CdTe solar cell. Reproduced with permission [151] Copyright 2022, Elsevier. (**b**) Stability of CdTe solar cell in function of etching cycles. Reproduced with permission [153]. Copyright 2017. Elsevier. (**c**) J–V curve of CIGS solar cell in function of modulated band gap. Reproduced with permission [165] Copyright 2020. Elsevier. (**d**) Stability of CIGS solar cells under short-circuit condition (SCC) and open-circuit condition (OCC). Reproduced with permission [166]. Copyright 2015. Elsevier.

Copper-Zinc-Tin Sulfide (CZTS)

CZTS has a similar structure to CIGS and offers the advantage of using abundant and non-toxic elements [167]. The CZTS solar cell structure typically consists of a molybdenum back contact, a CZTS absorber layer, a buffer layer, and a transparent conductive oxide front contact [168]. CZTS solar cells have lower PCE than CIGS solar cells, reaching values of up to 11.0% [169].

Copper-Zinc-Tin Selenide (CZTSe)

CZTSe solar cells operate in a similar manner to other thin-film solar cells. They consist of a substrate, a back contact, a CZTSe absorber layer, a buffer layer, and a transparent conductive oxide front contact [168]. CZTSe solar cells are like copper indium gallium selenide (CIGS) solar cells in terms of their crystal structure, which is a kesterite structure [170]. CZTSe has a higher bandgap than CIGS, which means that it can absorb a larger portion of the solar spectrum and potentially achieve higher efficiencies. CZTSe also has the advantage of being composed of earth-abundant and non-toxic materials. CZTSe solar cells face several challenges, such as low open-circuit voltage and fill factor due to the presence of defects and recombination centers in the absorber layer [171]. PCE currently reached values ~12.5% [172].

Cadmium-Free Copper Zinc Tin Sulfide (CZTSSe)

In cadmium-free CZTS solar cells, alternative cadmium sulfide. This allows for the elimination of toxic cadmium, resulting in a more environmentally friendly and sustainable solar cell technology [173]. CZTSSe solar cells have achieved PCE values of up to 12.6% [174].

Due to the fact that most of the fabricated chalcogenide devices do not report stability measurements, Table 4 shows a summary of the conversion efficiencies of the main solar cells of this generation and their corresponding parameters.

Table 4. Photovoltaic parameters of main chalcogenide-based solar cells.

Active Layer	J_{SC} (mA/cm^2)	V_{OC} (V)	FF	PCE	Ref.
CdTe	26.30	0.81	0.808	17.3	[151]
CdTe	30.25	0.87	0.794	21.0	[175]
CdTe	31.69	0.88	0.785	22.1	[106]
CIGS	39.80	0.72	0.765	21.8	[165]
CIGS	39.68	0.73	0.804	23.4	[163]
CIGS	39.33	0.73	0.805	23.3	[176]
CZTS	21.77	0.71	0.826	10.0	[177]
CZTS	21.74	0.73	0.693	11.0	[169]
CZTSe	38.30	0.46	0.663	11.8	[178]
CZTSe	37.40	0.49	0.682	12.5	[172]
CZTSSe	35.60	0.51	0.697	12.6	[174]
CZTSSe	35.20	0.51	0.698	12.6	[179]

2.2.2. Chalcogenide Tandem Solar Cells

Chalcogenide tandem solar cells have emerged as a promising candidate for achieving high-efficiency photovoltaic devices. In this type of solar cells, two or more different chalcogenide-based semiconductors with diverse bandgaps are assembled to absorb a broader range of the solar spectrum; see Figure 9a [180]. The upper cell absorbs the higher-energy photons, while the lower cell absorbs the lower-energy photons that pass through the upper cell [181]. This allows for a more efficient utilization of the solar spectrum and can lead to a higher overall efficiency. Chalcogenide-based materials, such as copper indium gallium selenide (CIGS), cadmium telluride (CdTe) [182], lead sulfide (PbS) [183,184] and earth-alternative materials such as kesterite-based chalcogenides [185,186] have been extensively studied for use in tandem solar cells. CIGS is particularly attractive due to its high absorption coefficient and tunable bandgap, making it suitable for use in both the top and bottom cells of the tandem device. Besides, CIGS tandem solar cells have high carrier mobility, scalability, potential for low-cost, and compatibility with alternative materials.

In recent years, perovskite-chalcogenide tandem solar cells have gained significant attention due to their high-power conversion efficiencies and potential for low-cost, scalable production [187–190]. Perovskites are inorganic materials that have unique optical properties. For more details, see Section 2.3. This kind of tandem solar cell typically combines a

perovskite material and other material as a different perovskite, CIGS and CdTe [191,192]. The perovskite material is used to absorb high-energy photons, while the other materials are used to absorb low-energy photons. High-energy photons absorbed by the perovskite generate electron-hole pairs. The electrons and holes then move to the interface between the perovskite and other material layers, where they are separated by a built-in electric field. The electrons flow through the bottom layer, while the holes flow through the perovskite layer, generating a photocurrent. The two currents are then combined at the electrode, producing a higher overall current than a single junction solar cell. These kinds of cells have a maximum efficiency of around 31% [106]. For instance, Al-Ashouri and workers [193] have fabricated a monolithic CIGSe/perovskite tandem solar cells, introducing the concept of self-assembled monolayers to choose suitable hole selective contacts and favor an efficient carrier separation/transport. For the optimized device, a maximum PCE of 23.26% was reached (Figure 9b) keeping the 97% of initial performance after 2400 h under operation; see Figure 9c. Table 5 shows different examples of tandem chalcogenide solar cell, their efficiencies, and parameters such as V_{OC}, J_{SC}, and FF.

Table 5. Photovoltaic parameters of main chalcogenide tandem solar cells.

| Active Layer	J_{SC} (mA/cm²)	V_{OC} (V)	FF	PCE	Stability	Ref.
Perovskite/CIGS	19.2	1.68	0.719	23.3	97% of initial performance, 2400 h, air	[193]
Perovskite/CIGS	19.24	1.77	0.729	24.2	-	[194]
DSSC/CIGS	14.6	1.17	0.77	13.0	67% of initial performance, 12 h	[180]
Perovskite/PbS	-	-	-	20.3	90% of initial performance, 12.5 h, without encapsulation	[195]
Perovskite/Perovskite	16.0	2.01	0.800	25.6	88% of initial performance, 500 h, air	[196]
CuInSe$_2$/Perovskite	12.9	1.34	0.635	11.0	~70% of initial performance, 2400 h, in a desiccator	[197]
Perovskite/PbS	16.67	1.79	0.783	23.4	-	[198]
GaInP/AlGaAs/CIGS	11.72	2.95	0.818	29.1	90% of initial performance, after 50 cycles of operation	[199]
GaAs$_{0.75}$P$_{0.25}$/Si	20.47	1.91	0.798	31.3	-	[200]
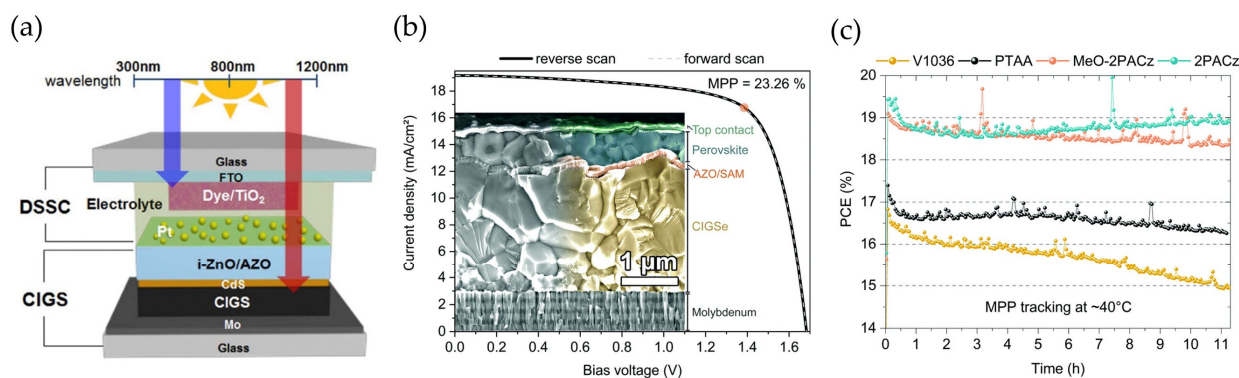
Figure 9. (**a**) Representation of a tandem solar cell based on a DSSC/CIGS assembly. Reproduced under the terms of the CC-BY license [180]. Copyright 2015. The authors. Springer Nature. (**b**) J–V curve and (**c**) stability measurements of a tandem perovskite-CIGS solar cell. Reproduced under the terms of the CC-BY license [193]. Copyright 2019, The authors, Royal Society of Chemistry.

2.2.3. New Chalcogenide Materials

II-IV-N$_2$ materials such as MgSnN$_2$ (MTN) and ZnSnN$_2$ (ZTN) are being investigated for their potential as absorber layers in solar cells [201,202]. Both materials are nitrides that belong to the wurtzite crystal structure and are composed of earth-abundant elements [203]. MTN and ZTN have bandgap energies in the visible range, making them well-suited for solar absorption [203]. They also have high carrier mobility, which is important for efficient charge transport in solar cells [203]. However, there are still challenges to the manufacture of these materials. For instance, to create high-quality thin films of MTN and ZTN high-temperature growth techniques such as molecular beam epitaxy or metalorganic chemical vapor deposition are used, which can be expensive and difficult to scale up for large-scale production. Moreover, the properties of the films can be sensitive to the growth conditions,

leading to variations in their electronic and optical properties. Another challenge is the development of suitable heterojunctions and contacts for efficient charge collection in solar cells based on MTN and ZTN. Several studies have explored the use of different materials, such as graphene or molybdenum disulfide, as contacts for MTN and ZTN solar cells, but further research is needed to optimize their performance. Efficiencies of ZTN solar cells reach 1.5% [204], which is still low compared to conventional solar cells.

Antimony chalcogenides (Sb_2X_3, where X is a chalcogen element such as sulfur, selenium, or tellurium) have recently gained attention as potential materials for solar cell applications due to their advantageous optoelectronic properties such as high absorption coefficients and suitable bandgap energies for solar energy conversion [205]. One advantage of using antimony chalcogenides is that they are relatively abundant and less toxic compared to other chalcogenide materials such as cadmium telluride (CdTe) [206]. Additionally, antimony chalcogenides have shown promising photovoltaic efficiencies, with reported values ranging from 2% to 10.7% for various device structures [207,208]. However, challenges remain for antimony chalcogenide-based solar cells, including issues related to material stability and durability. For example, Sb_2Se_3 is prone to degradation when exposed to moisture and air, which can limit its practical application. Furthermore, antimony chalcogenides have relatively low carrier mobilities, which can affect device performance [209,210].

2.3. Halide Perovskite Based Solar Cells

2.3.1. Pb-Based Perovskites Active Layers

Since Miyasaka and coworkers integrated HPs as promising light harvesters to provide a step forward in a new generation of solar cells in 2009 [211], these materials have been consolidated as the most prominent semiconductors for photovoltaics. Typically, HPs show a 3D structure based on ABX_3 formula (A = Cs^+, cesium; MA^+, methylammonium; FA^+, formamidinium; B = Pb^{2+}, Sn^{2+}; X = Cl^-, Br^-, I^-, or combinations), where the composition and particle size engineering can promote the preparation of HPs with diverse photophysical, chemical, and electronic properties [212–214]. Due to the fact that a solar device should collect as much incident illumination as possible in a broad range of the energy spectrum to reach an efficient light-to-current transformation, low-band gap HPs are ideal for this process. Therefore, HPs with high iodide content are in the focus of many research groups, obtaining different strategies to reach a suitable active layer, compatible and stable with the selective contacts of the solar cell, to facilitate the carrier mobility through the device [215,216]. Although an acceleration in the number of publications have been reported to show current alternatives to prepare adequate HPs active layers (open the door to an extensive number of reviews), here, we will highlight some of these contributions where the modification of the perovskite layer has been vital to increasing the performance of the solar devices.

Similar to the generations of solar devices shown above, PSCs are composed by an electron transporter layer (ETL) and hole transporter layer (HTL), which favor the carrier transport through the device [217]. Moreover, a transparent conducting glass as fluorine-doped tin oxide (FTO) is used to promote the carrier mobility and allow the direct illumination of the active layer, while on top of the PSC architecture, metals such as silver or gold are deposited [218]. As we previously mentioned, iodide HPs are the most relevant photomaterials to achieve a high photoconversion efficiency (PCE) in PSCs, especially perovskites based on $FAPbI_3$. This material presents a band gap around 1.4 eV, indicating a broad absorption capability of solar energy in the UV-vis-NIR spectrum [219–221]. This band gap value also corresponds to a theoretical PCE ~32.3%, near to the Shockley–Queisser limit of efficiency [222]. Unfortunately, this feature is achieved for the photoactive phase of the $FAPbI_3$, denominated as black α-phase, which is stable at high temperatures, but is eventually transformed into the yellow δ-phase at room conditions; see Figure 10a [223]. To suppress the fast α-to-δ phase conversion into this kind of perovskite, Meng and coworkers [224] have prepared bulk films based on $FA_{0.94}MA_{0.06}Pb(I_{0.94},Br_{0.06})_3$, which have been coupled with carbon electrodes on top, in a n-i-p device configuration, to accelerate the

carrier separation and transport into the fabricated solar cell. Here, bromide anions were incorporated into the perovskite to provide better stability to the material since iodide species are more labile, being rapidly diffused from the perovskite lattice to create structural defects. However, the presence of Br also offers the enlargement of the band gap, hampering the sunlight absorption capability of the perovskite. In this context, a high FA content ~94% was introduced into the material, to guarantee a narrow band gap. Attending to the final device, the PCE was estimated to be 20.04% at 1 sun illumination. At this point, the 94% of the initial performance of the solar cell was maintained for 1000 h.

On the other hand, Kim and coworkers [225] have deeply investigated the impact of the addition of MACl as an additive for the stabilization of FAPbI$_3$ to obtain highly-performance solar cells. Here, they demonstrated that the α-to-δ phase transition is promoted by the weak interaction between FA$^+$ cations and the iodide species from the [PbI$_6$]$^{4-}$ octahedra building blocks, which is one of the key factors to trigger the octahedra tilting [226–228]. Thus, the presence of Cl provides a better p orbital localization from I, improving the FA-I interactions beyond compensating halide vacancies into the perovskite structure. Then, MA$^+$ cations also facilitate the perovskite stabilization, causing a contraction of the cubo-octahedra sites in the material. MA$^+$ shows a higher dipolar moment than that of FA cations (~10 times), strengthening the volume shrinkage, making closer a direct interaction between FA and I. Therefore, authors have estimated a PCE ~24% (under 1 sun) in the devices containing the mixed cation FA/MA-perovskites, keeping 90% of their initial performance after 1200 h of operation. In this context, it is well known that the lattice distortion of the perovskites negatively impacts the net performance of the PSCs, favoring the emergence of non-radiative recombination traps, hindering the carrier transport into the fabricated device [227,229]. Thus, it is suitable to decrease the level of local strain into the perovskite structure to increase the PCE and thereby, extend the device stability. In these studies, Seok and coworkers [230] have proposed the combination of A-site cations to replace some FA$^+$ species from the FAPbI$_3$ and delay the phase conversion of its photoactive black α-phase. Here, a dual substitution of FA$^+$ by larger methylenediammonium (MDA^{2+}) and small Cs$^+$ cation in a same molar ratio (0.03 mol fraction) relaxes the lattice strain into the perovskite (denominated as (FAPbI$_3$)$_{1-x}$(MC)$_x$) also contributing to suppress the carrier traps and improving the radiative recombination pathway in the photomaterial. At this point, a maximum PCE ~25.2% was achieved in fabricated PSCs under 1 sun illumination; see Figure 10b, keeping 80% of their initial efficiency for 1300 h, at 85 °C; see Figure 10c. In addition, Seok's research group have introduced some alkylammonium chlorides (RACl) as the case of propylammonium and butylammonium chloride to improve the crystallinity and compensate for structural defects contained into the FAPbI$_3$ based HPs [42]. Here, a maximum PCE of 26.08%, retaining over 88% of the initial efficiency for 600 h under operation.

To date, the octahedral tilting is induced by the loss of halide species such as iodide anions during the perovskite film preparation [223,231,232], generating a high density of halide vacancies (thereby, high density of carrier traps is produced), leading to the degradation of the photophysical and electronic features of the material. More specifically, the I$^-$ anions released from the perovskite structure are easily oxidized to obtain I^0, which is the main species to trigger chemical chain reactions and accelerate the quenching of the intrinsic properties of the active layer [232]. For this purpose, different organic agents have been introduced to avoid the formation of halide vacancies and strengthen the Pb-I bonds in the octahedra building blocks, as in the case of caffeine [233], theobromine [234], alkylammonium halides [234], phosphonopropionic acid [235] and some amino-based organic ligands [236]. Although some of these organic agents show a high binding capability to the [PbI$_6$]$^{4-}$ octahedra units, avoiding the halide deficiency, they also exhibit fast decomposition under heating or can acts as barrier layers (due to their long carbon chains). This fact hinders the carrier extraction from the perovskite, hampering the net performance of the solar device. Therefore, with the purpose of reducing the iodide migration and thereby inhibit the formation of halide defect sites in the perovskite layer, Zhao and coworkers [237]

have added 3-amidinopyridine (3AP) during the material preparation, inducing the coordination between amidino moieties and the Pb-I frameworks. In this scenario, a maximum PCE of 25.3% was obtained in optimized PSCs under 1 sun irradiation, preserving ~92% of the initial efficiency for 5000 h in ambient air.

Other alternatives to stabilize the perovskite active layer have been focused on the direct incorporation of large alkylammonium species to react with the 3D HPs to form multidimensional 2D/3D systems with longer durability [236,238,239]. Considering that big cations do not match with the Goldschmidt tolerance factor, breaking the 3D preferential crystalline structure of the perovskite, the $[PbX_6]^{4-}$ octahedra in form of stacking layers are separated by these of organic agents [240,241]; see Figure 10d. The 2D perovskites are environmentally stable and promote Vander Waals interactions with the Pb-X frameworks. However, these materials exhibit a large band gap and poor carrier transport capability, decreasing the PCE in modified PSCs. In this way, it is favorable the mixture of 2D/3D systems to facilitate the separation/mobility of electrons through the device. Grancini and coworkers [242] have proposed the incorporation of 2-thiophenemethylammonium halides, 2-TMAX (X = Cl, Br and I) during the preparation of triple-cation $[(FAPbI_3)_{0.87}(MAPbBr_3)_{0.13}]_{0.92}(CsPbI_3)_{0.08}$ perovskite, where the thiophene organic species react with the photomaterial to create the 2D layer. By adding 2-TMABr and 2-TMAI agents, a suitable band structure (valence band shift) in between the 2D-3D perovskites is mediated, favoring the hole extraction into the heterojunction, contrary to 2-TMACl, where the carrier diffusion was hampered. Accordingly, PSCs with a maximum PCE of 20.8% (under 1 sun) were fabricated, keeping 74% of their initial performance for 1000 h of operation without any encapsulation. Another example is mentioned by Zhou and coworkers [241], where the 2-thiophenemethylammonium (ThMA) spacer was also added during the preparation of FA/MA based 3D perovskite. Here perovskite crystals were orientally grown, inducing the passivation of a high density of carrier traps to avoid the non-radiative recombination losses. Here, devices provided high PCE up to 21.5%; see Figure 10e, preserving 99% of its initial performance after 1680 h ambient air; see Figure 10f.

Then, a mixture of organic spacers such as iso-butylammonium iodide (i-BAI) and FA-iodide (FAI) reported by Cho and coworkers [243] suppressed the interfacial carrier traps and thereby reduced the interfacial energy barrier to avoid carrier diffusion. A PCE as high as 21.7% was obtained for the optimized solar device, keeping 87% of the original efficiency after 912 h with a relative humidity of 75%.

To maximize the absorption ability and electronic features of the bulk HPs, these materials have also been integrated with other types of solar devices such as Si, copper indium gallium selenide, different PSCs, DSSCs and QDs-based solar cells to fabricate tandem devices, as shown above [192]. Some works have reached near to 30%, as the case of the contribution reported by Albrecht and coworkers [244], where a monolithic perovskite tandem solar cell (PTSC) was fabricated. Here, a wide-band gap $Cs_{0.05}(FA_{0.77}MA_{0.23})_{0.95}Pb(I_{0.77}Br_{0.23})_3$ bulk film was integrated with a Si-based solar device, also incorporating diverse hole transporter layers such as C_{60}, 2PACz and Me-4PACz, to accelerate the carrier extraction. A maximum of PCE ~29% was achieved for the optimized PTSC, retaining the 95% of the initial performance after 300 h under operation. Interestingly, De wolf and coworkers [245] have incorporated MgF_2 as an interlayer between the perovskite based on triple cation $Cs_{0.05}FA_{0.8}MA_{0.15}Pb(I_{0.755}Br_{0.255})_3$ and C_{60} to improve the electron extraction (better adjustment of the relative energy positions in the perovskite) and separate the C_{60} from the active layer surface to restrain the non-radiative recombination dynamics. Accordingly, a stabilized PCE of 29.3% was achieved, where the optimized PTSC device retained ~95% of its initial performance after 1000 h of operation, even carrying out damp-heat testing at 85 °C with 85% relative humidity. Recently, this research group provided a new record of the PCE ~33.2% using a similar perovskite layer on top of the cell, while a textured Si solar device is in the bottom of the configuration.
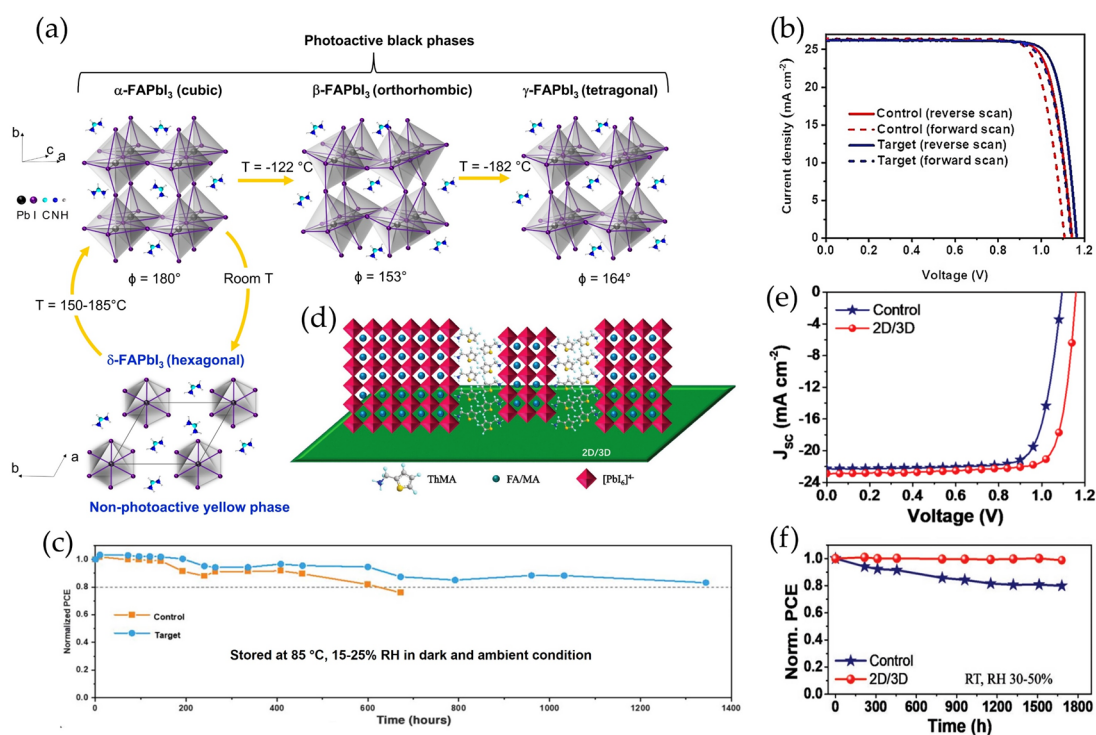
Figure 10. (**a**) Typical phase transformation of the FAPbI$_3$ crystalline structure. The δ–to–α phase transition is promoted at high temperature. Reproduced with permission [223]. Copyright 2020. American Chemical Society. (**b**) Performance and (**c**) long-term stability measurements of the (FAPbI$_3$)$_{1-x}$(MC)$_x$ (x = 0.03 mol%) and control–based PSCs (uncapsulated devices). Reproduced with permission [230]. Copyright 2020. Science AAAS. (**d**) Schematic of the proposed 2D/3D FA/MA perovskite film where ThMA spacer is incorporated between the [PbI$_6$]$^{4-}$ octahedra layers, which is perpendicular to the substrate. (**e**) Performance and (**f**) stability test of the control and 2D/3D FA/MA–based PSC. Reproduced with permission [241]. Copyright 2019. John Wiley & Sons, Inc.

Even though the surface passivation with interesting alkylammonium ligands and the incorporation of 2D/3D heterostructures enhance the operational performance of the solar devices, it is reasonable that some differences in the PCE values are obtained. So, the highest PCE value is reached by filling/replacing structural defects in the active layer, improving its optical and electronic properties, suppressing carrier traps, and facilitating carrier transport. Although 2D/3D assembly can also achieve defect passivation in the perovskite, the appearance of a heterostructure can promote the emergence of interfacial energy levels where the carriers can be trapped, hampering the development of a higher device efficiency.

2.3.2. Partially Pb-Substituted/Pb-Free Perovskite Active Layers

As we have highlighted above, a series of approaches are prominent to reach long-term stability and suitable electronic properties in perovskites to favor carrier separation/extraction and mobility through the fabricated device. However, it is also known that one of the main drawbacks of the PSCs is the inherent toxicity of Pb, which hampers the future commercialization of this technology [246,247]. Therefore, the fact of substituting Pb partially or completely with less toxic metals, preserve/increase the final properties of the active layer, and thereby, reaching high performance in the solar device, is still a huge challenge. One of the most attractive metals to replace Pb is Sn, which also generate [SnX$_6$]$^{4-}$ octahedra units to generate multidimensional HPs structures as the case of Pb and provide HPs lower band gap than that of Pb-analogous [248]. Nevertheless, Sn-HPs exhibit a poor stability consequence of the fast Sn^{2+}-to-Sn^{4+} oxidation under ambient conditions, degrading the net efficiency in solar devices [249,250]. Hence, we will focus on the

fabrication of PSCs based on a mixture of Sn/Pb- or Sn-HPs introducing novel strategies to avoid Sn oxidation in the active layer and thereby increase the performance of Sn-PSCs.

Firstly, for Sn/Pb-HPs systems, Wang and coworkers [251] have studied the addition of antioxidants such as tea polyphenol (TP) during the preparation of optimized $CsPb_{0.5}Sn_{0.5}I_2Br$ bulk film to avoid the rapid Sn oxidation. Through the coordination bonds between high Lewis acidity Sn sites and hydroxybenzene groups, the Sn^{4+}/Sn^{2+} ratio into the HP was decreased from 68.1% to 5.85%, deducing that TP is a good reducing agent. In addition, this antioxidant mediated an improved HP crystallization, making that at 0.5 wt% TP, a homogeneous film with a low content of pinholes is obtained. Therefore, low density of grain boundaries appears to hinder the carrier extraction. A maximum PCE of 8.1% was reached under 1 sun illumination, retaining 95% of original performance after ~1440 h into a N_2-filled glove box. Meanwhile, Guo and coworkers [252] have used the mixture of 2D/3D HPs in order to prepare suitable heterostructures for PSCs. Here, authors have introduced bulky alkylammonium based on 2-(4-fluorophenyl)ethylammonium iodide (FPEAI) during the preparation of $(MAPbI_3)_{0.75}(FASnI_3)_{0.25}$ films. In presence of the organic cation, highly oriented crystals are grown, and phase segregation occurring as the result of the Sn oxidation (emerging two distinguished signals from $MAPbI_3$ and $FASnI_3$ HPs), is suppressed. This fact makes that the recombination lifetime is longer than that of the absence of the organic molecules, associated with the reduction of high density of trap states. In context, a high PCE of 17.51% was reached (Figure 11a), keeping 90% of the initial performance after 1200 h into a glove box (Figure 11b), and 70% of initial efficiency close to 400 h under ambient air; see Figure 11c.
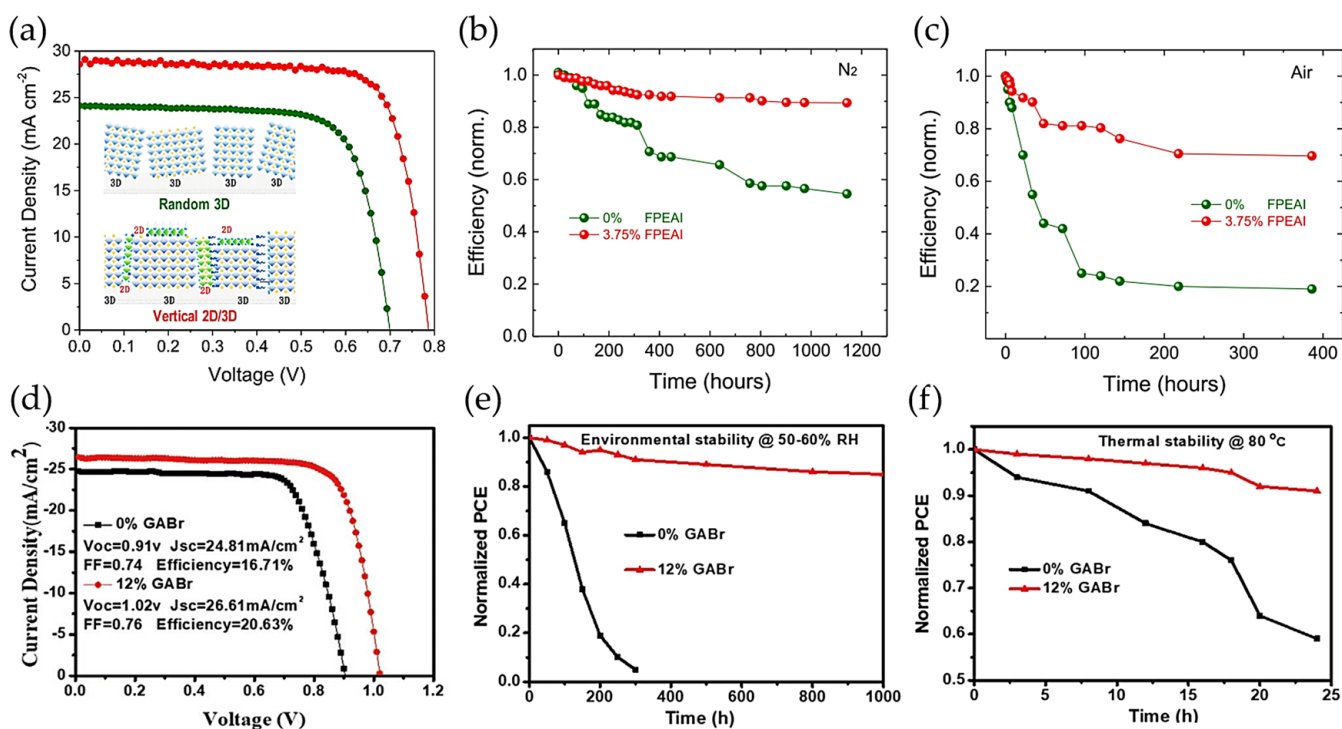

Figure 11. (**a**) Photovoltaic performance of the optimized $(MAPbI_3)_{0.75}(FASnI_3)_{0.25}$ PSC in presence and absence of 3.75 wt% FPEAI. Stability measurements for the Sn/Pb-based PSCs with and without the FPEAI additive under (**b**) N_2 atmosphere and (**c**) in ambient air. Inset of Figure 4a shows the randomly oriented 3D HP structure, which is vertically aligned in presence of the FPEAI organic agent. Reproduced with permission [252]. Copyright 2020. American Chemical Society. (**d**) Performance, (**e**) environmental and (**f**) thermal stability measurements of the 2D/3D $FA_{0.7}MA_{0.3}Pb_{0.7}Sn_{0.3}I_3$-based PSCs in presence and absence of 12% wt GABr. Reproduced with permission [253]. Copyright 2020. John Wiley & Sons, Inc.

Then, Xu and coworkers [253] employed the surface passivation concept to prolong the stability of the $FA_{0.7}MA_{0.3}Pb_{0.7}Sn_{0.3}I_3$ HPs and remove structural defects from the material using guanidinium bromide (GABr). Considering that GA^+ cations provide more charge density than FA^+ and MA^+ cations, this could be one of the main explanations to restrain the fast Sn^{2+}-to-Sn^{4+} transformation. In addition, iodide vacancies are formed by the depletion of Sn^{2+}, creating high content of halide vacancies into the perovskite. Thus, Br^- domains fill/replace these empty states to enhance the final properties of the prepared active layer. The optimized device has reached a maximum PCE of 20.63% without any encapsulation; see Figure 11d, conserving over 85% of the original efficiency after 1000 h under ambient air; see Figure 11e, and 80% of the original efficiency after 24 h of operation at 80 °C; see Figure 11f. Lastly, Huang and coworkers [245] have demonstrated that the addition of an alkylammonium pseudo-halide additive based on octylammonium tetrafluoroborate ($OA^+BF_4^-$) for the preparation of MA-free Sn/Pb HPs. While OA^+ cations can fill some A-site cations into the HPs, BF_4^- species compensate the iodide vacancies generated by the Sn oxidation, also reducing the likelihood of emerging interstitial iodide and iodine. The suppression of defect density, main factor to promote carrier trapping, facilitates the fabrication of PSCs with PCE up to 23.7% (a record for Sn/Pb-PSCs), keeping over 88% of the initial performance after 1000 h of continuous operation at 50 °C in air and tracking the device under MPP.

For the case of the stabilization of Sn-based PSCs, some examples can be addressed. Mora-Seró and coworkers [254] have made use of the chemical engineering strategy, where Dipropylammonium iodide (DipI) and sodium borohydride ($NaBH_4$) (known as a good reducing agent) have been added to the preparation of $FASnI_3$ films and prevent the Sn oxidation. While DipI can block the loss of iodine in form of I_2, $NaBH_4$ reduce the released I_2 to produce iodide into the HPs, avoiding the halide migration. Therefore, the Sn^{2+}/Sn^{4+} and I^-/I_2 ratios are increased, inhibiting the formation of interstitial iodine/iodide vacancies, which are the main energy states where the hole/electrons can be trapped. In this alternative for stabilizing Sn, optimized devices boost a high PCE of 10.61%; see Figure 12a, providing up to 96% of the initial performance after 1300 h of continuous operation at MPP in N_2 condition; see Figure 12b,c. Another approach to stabilizing the black phase of the $FASnI_3$, Mi and coworkers [255] have introduced trimethylthiourea (3T) during the spin-coating process for HPs preparation. The presence of this bifunctional ligand induces coordination bonds with Sn^{2+} cations through the formation of Sn-S species. Simultaneously, N-H moiety from the organic agent produces hydrogen bond iodide species from the octahedra building blocks to avoid their diffusion out from the HPs lattice. Due to these effects, the carrier recombination is prolonged in comparison to the pristine HPs, hindering the emergence of carrier traps. In this context, PSCs were able to develop a maximum PCE up to 14%, maintaining 100% of the original efficiency for more than 700 h, under N_2 atmosphere. On the other hand, He and coworkers [256] have included 4-fluoro-phenethylammonium bromide (FPEABr) into the precursor solution to prepare 2D/3D Sn-HPs with low density of structural defects. FPEA cations are incorporated into the perovskite surface, while F- and Br-anions fill/replace halide vacancies. In terms of the device architecture, the 2D Sn-perovskite acts as an interface layer between the active layer and PEDOT:PSS hole transporter layer, restraining the iodide migration into the device. In presence of 10 wt% FPEABr, encapsulated 2D/3D PSCs generate a PCE up to 14.81%; see Figure 12d, exhibiting over 80% initial performance after 432 h under operation at room temperature (Figure 12e), and 60% of initial efficiency after 1 h at 80 °C (Figure 12f), both kinds of tests under ambient air.
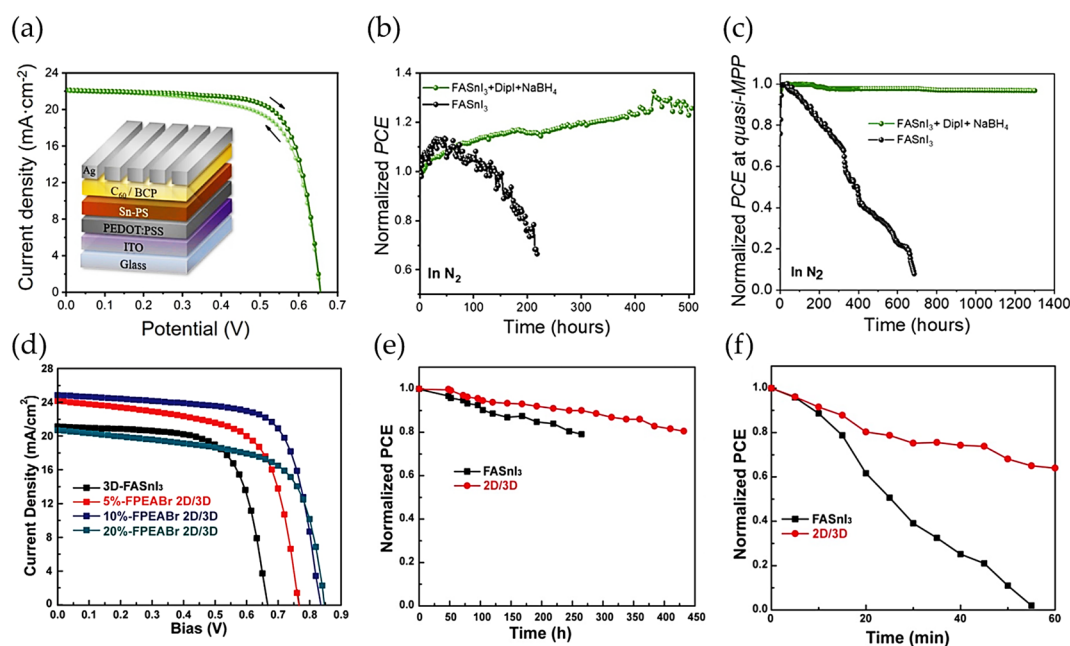
Figure 12. (**a**) Photovoltaic performance of the FASnI₃-based PSCs in presence of DipI/NaBH₄. Inset of Figure 5a exhibits the architecture of the optimized device. Stability measurements of the FASnI₃ devices in presence and absence of the additives (**b**) under N₂ atmosphere and (**c**) at MPP under inert conditions. Reproduced with permission [254]. Copyright 2022. Elsevier. (**d**) Photovoltaic performance of the FASnI₃ PSCs by varying the amount (wt%) of FPEABr to prepare the 2D/3D structure. Stability measurements of the FASnI₃ and 2D/3D perovskite-based PSCs (**e**) at room temperature and (**f**) at 80 °C, both set of measurements under ambient air. Reproduced with permission [256]. Copyright 2021. John Wiley & Sons, Inc.

Table 6 shows the comparison in photovoltaic performances of the above perovskite-based solar devices, providing main parameters, such as J_{sc}, V_{oc}, and FF, to estimate the corresponding PCE. It is evident that PSCs fabricated with Pb-based HP films are more stable and still offer a high performance, mainly associated to hampered oxidation condition of Pb itself. However, even though the net efficiency offered by Sn/Pb- or Sn-PSCs are lower compared to their Pb-analogous, diverse alternatives are presented to improve their long-stability in room conditions (inhibiting the fast Sn oxidation), which is pivotal to finding the suitable conditions to increase the PCE in future Pb-free PSC technologies.

Table 6. Summary of photovoltaic parameters of the optimized devices based on Pb-, Sn/Pb-, Sn-perovskite films.

Pb-Based Perovskite Films						
Active Layer	J_{sc} **(mAcm^{-2})**	V_{oc} **(V)**	**FF**	**PCE (%)**	**Stability**	**Ref.**
FA$_{0.94}$MA$_{0.06}$Pb(I$_{0.94}$,Br$_{0.06}$)$_3$	23.60	1.11	0.765	20.04	94% of initial performance, 1000 h, air	[224]
FAPbI$_3$–40 wt% MACl	25.92	1.13	0.820	24.02	90% of initial performance, 1200 h, air	[225]
(FAPbI$_3$)$_{1-x}$(MC)$_x$, x = 0.03 mol%	26.23	1.17	0.822	25.20	80% of initial performance, 1300 h, 85 °C, air	[230]
FAPbI$_3$–10 mol% RACl	25.69	1.18	0.862	26.08	88% of initial performance, 600 h, air	[42]

Table 6. *Cont.*

Pb-Based Perovskite Films						
Active Layer	J_{sc} **(mAcm^{-2})**	**V_{oc} (V)**	**FF**	**PCE (%)**	**Stability**	**Ref.**
FAPbI$_3$–4 mol% 3AP	26.04	1.18	0.822	25.30	92% of initial efficiency, 5000 h, air	[237]
2-TMABr–modified (FAPbI$_3$)$_{0.87}$(MAPbBr$_3$)$_{0.13}$]$_{0.92}$(CsPbI$_3$)$_{0.08}$	23.20	1.15	0.780	20.80	74% of initial efficiency, 1000 h, air	[242]
ThMA–modified 2D/3D FA/MA perovskite	22.88	1.16	0.810	21.49	99% of its initial performance, 1680 h, air	[241]
i-BAI/FAI–modified (FAPbI$_3$)$_{0.85}$(MAPbBr$_3$)$_{0.15}$	~23	~1.18	~0.825	21.70	87% of the original efficiency, 912 h, air	[243]
Cs$_{0.05}$(FA$_{0.77}$MA$_{0.23}$)$_{0.95}$Pb(I$_{0.77}$Br$_{0.23}$)$_3$/Si PTSC	19.26	1.90	0.795	29.05	95% of the initial performance, 300 h, air	[244]
MgFx–modified Cs$_{0.05}$FA$_{0.8}$MA$_{0.15}$Pb(I$_{0.755}$Br$_{0.255}$)$_3$	20.58	1.92	0.807	29.30	95% of the initial performance, 1000 h, 85 °C, air	[245]
Partially Pb-Substituted/Pb-Free Perovskite Films						
Perovskite Layer	J_{sc} **(mAcm^{-2})**	**V_{oc} (V)**	**FF**	**PCE (%)**	**Stability**	**Ref.**
TP–modified CsPb$_{0.5}$Sn$_{0.5}$I$_2$Br	20.10	0.62	0.650	8.10	95% of original performance, ~1440 h, N$_2$–atmosphere	[251]
(MAPbI$_3$)$_{0.75}$(FASnI$_3$)$_{0.25}$–3.75 wt% FPEAI	28.42	0.79	0.780	17.51	90% of the initial performance, 1200 h N$_2$–atmosphere, 70% of initial efficiency, 400 h, air.	[252]
FA$_{0.7}$MA$_{0.3}$Pb$_{0.7}$Sn$_{0.3}$I$_3$–12 wt% GABr	26.61	1.02	0.760	20.63	85% of original efficiency, 1000 h, air 80% of original efficiency, 24 h, 80 °C, air	[253]
OABF$_4$–modified Cs$_{0.2}$FA$_{0.8}$Pb$_{0.5}$Sn$_{0.5}$I$_3$	33.80	0.88	0.800	23.70	88% of initial performance, 1000 h, continuous operation at 50 °C, air, tracking under MPP	[245]
DipI/NaBH$_4$–modified FASnI$_3$	22.13	0.65	0.731	10.61	96% of initial performance, 1300 h, continuous operation at MPP, N$_2$-atmosphere	[254]
3T–modified FASnI$_3$	20.50	0.91	0.757	14.06	100% of original efficiency, >700 h, N$_2$–atmosphere	[255]
FPEABr–modified 2D/3D FASnI$_3$ (10 mol%)	24.91	0.84	0.708	14.81	80% of initial performance, 432 h, continuous operation, air 60% of initial efficiency, 1 h at 80 °C, air	[256]

After describing the main characteristics of each kind of active layer used to fabricate the corresponding solar devices, some advantages and disadvantages of the related systems can be compared. Even aromatic moieties can promote carrier mobility in the organic sensitizers; carrier extraction is facilitated by the preparation of bulk heterojunctions, where an organic carrier acceptor and donor are assembled. Nevertheless, the formation of these heterostructures produce inhomogeneous morphology of the active layer, being of the critical reasons to favor the carrier recombination and the decrease in the PCE of the OSCs. In this line, chalcogenides were then integrated for the fabrication of more innovative solar devices, where the carrier injection depends on the relative energy positions of these kind of sensitizers, which can be modulated through material composition or particle size. Unfortunately, chalcogenides are prone to photocorrosion, damaging their optical and

electronic properties. Under this view, it seems that halide perovskites are the unique and most prominent option to be incorporated as active layer for solar cells, taking into account their high absorption coefficient, better electronic properties and versatile surface chemistry. However, some reports and review articles disagree with the former qualification, attending to the fact that the ionic structure of perovskites is highly labile, generating high density of defect sides, which decreases the stability of the photomaterial. Therefore, one interesting question emerges at this point: what is the suitable active layer to produce a solar device with high light-harvesting capability, efficient PCE with long-term stability? According to the results exposed through the different operational parameters of each generation of solar cells (Tables 1–6), the tandem systems are the most promising devices to have an important impact in photovoltaics, covering the absorption of the light in a broad range of the energy spectrum (UV-vis-NIR) by integrating wide- and narrow-band gap active layers (from diverse generation of solar cells), improving carrier generation/separation and diffusion. At this scenario, these types of devices offer one step forward the commercialization of solar technologies and are competitive against the well-established Si-based solar cells.

3. Concluding Remarks

This review shows the different generations of solar cells, considering the most important advances in the preparation of efficient active layers (organic, chalcogenide and halide perovskites) with improved capability to harvest most of the solar energy spectrum and promote the photocarrier transport into the solar device. As highlighted first, dye sensitizers were the first low-cost active layers to be incorporated with the purpose of replacing conventional and expensive silicon-based solar cells, taking advantage of their good absorption coefficient and facile carrier extraction. However, most of the organic materials show optical properties at specific wavelengths, hindering the photocarriers generation and lowering the PCE values. Therefore, organic molecules or species based on phthalocyanine and perylene derivatives have gained growing interest and are being integrated into novel OSCs. This fact provides the opportunity to achieve a better light harvesting performance and increase the density of carriers flowing into the device. Then, highly conductive materials such as fullerenes, and the concept of "bulk heterojunction" have been taken advantage to enhance the electron diffusion into the solar cell component interfaces, facilitating the photocarrier separation. Unfortunately, the inhomogeneity in the morphology of the organic active layers and their relatively fast deterioration make the density of carrier traps increase, hindering the electrons reach the external circuit of the solar cell. Here, the best OSCs can achieve PCE of more than 20% recently, but low stability in the range of hours can be achieved.

To overcome the above issues, chalcogenide-based solar cells have emerged to expand the light absorption capability of the active layer in a broad range of the energy spectrum (with a higher absorption coefficient than organic sensitizers), also considering the multiple pathways to prepare suitable films for efficient device prototypes. In this way, by attending to the chemical composition of the metal chalcogenides such as CdTe, PbS or some of them with metal combinations to obtain CZTSe/CZTSSe derivatives, light harvesting in the IR range is unlocked to provide more photocarriers, and thereby, more photocurrent is developed. Moreover, p-type and n-type chalcogenides can be assembled to offer an adequate band structure with electron and hole transporting layers, promoting effective carrier injection and mobility through the solar cells. Accordingly, PCE values close to 25% can be reached, also enhancing the stability of the device for long time of operation, even under harsh conditions such as H_2O, O_2, and high temperatures. Nevertheless, some disadvantages, such as high resistance for carrier mobility, the appearance of high density of energy traps favoring the surface recombination, and the use of toxic elements such as Cd, S, Te among others, decrease the possibility of using chalcogenides for further improvements in device performance.

Attending to the latter, HPs active layers have emerged as the most prominent semiconductors, gaining attention in photovoltaics due to their exponential enhancement in

light-to-electricity transformation capability is some couple of years. Because of their versatile surface chemistry and variable composition, intrinsic properties of perovskites such as band gap can be easily modifiable, in order to improve the material stability without modifying their photoactivity. In this context, diverse strategies to delay the α-to-δ phase transformation in iodide-HPs have been applied in order to decrease the density of structural defects (main reason to promote the octahedra titling and thereby favoring the phase transition), preserve the optical performance and restrain the carrier recombination dynamics. Mainly, bulky organic cations are introduced to prepare 2D/3D perovskite systems, where a suitable heterojunction is established to facilitate the carrier extraction. In addition, the introduction of alkylammonium halides is pivotal to suppress halide deficiency (carrier traps), contributing to the carrier diffusion to the external circuit of the cell, increasing the net efficiency of the solar cell. Therefore, PCE values higher than 25% have been reached, with long-term stability for hours in air ambient, being competitive with recent Si-based devices. However, like chalcogenides, inherent toxicity of HPs is found due to the presence of Pb, one of the main explanations to hinder their future commercialization. Therefore, partially Pb-substituted/Pb-free HPs have been prepared replacing Pb instead of Sn, including promising additives to prevent the progressive oxidation of the metal. Even the net performance of Sn-based HPs layers is not so high compared to their Pb-analogous, long-term stability under ambient air has been analyzed, being the first step to find the device parameters with the purpose to increase the operational efficiency. Attending to the fact that innovative strategies are being studied to produce a more stable photomaterial with good optical performance and stability, the use HPs have reached an exponential interest during recent years, establishing them as the most prominent active layers to fabricate solar cells. Unlike organic sensitizers and metal chalcogenides, the facile control of the surface chemistry of HPs, mainly surface passivation, make them versatile materials with improved intrinsic properties, even to be applied in other interesting research topics such as optoelectronics, solar-driven chemical reactions and so on.

From the perspective of developing solar devices with maximum photovoltaic performance, the combination of different generations of solar cells to fabricate tandem devices will be the most rentable/profitable option to maximize sunlight absorption, carrier photogeneration, and transport, due to the use of wide-band gap and narrow-band gap active layers, increasing the density of electrons to flow through the cell. At this point, matching the relative energy positions of the components into the device provides the suitable pathway for the carrier injection and mobility, avoiding the carrier trapping. On the other hand, the partial or total replacement of toxic metals, such as Cd of Pb from chalcogenides and perovskites, respectively, are recently one of the top research challenges to provide a step forward to future commercialization and being competitive with Si-solar cells. In this way, some ultrathin or flexible perovskite devices could be competitive with the recent state-of-the art. Without a doubt, more prominent works will be focused on this topic, preserving of increasing the optical performance, operational efficiency, and stability of innovative devices. This contribution gives an insight about the different active layers useful to continue future studies in photovoltaics and fabricate more efficient, less toxic, and stable devices with promising potential to compensate for energy consumption in the coming years.

Author Contributions: Conceptualization, writing—original draft preparation, writing—review and editing, F.W., C.S., J.M., I.O.-R., S.J.Y., D.J. and A.F.G.-R. Supervision, A.F.G.-R., F.W. and C.S. have equally contributed on this work. All authors have read and agreed to the published version of the manuscript.

References

1.　Fthenakis, V.M. End-of-Life Management and Recycling of PV Modules. *Energy Policy* **2000**, *28*, 1051–1058. [CrossRef]
2.　Carneiro, A.L.; Martins, A.A.; Duarte, V.C.M.; Mata, T.M.; Andrade, L. Energy Consumption and Carbon Footprint of Perovskite Solar Cells. *Energy Rep.* **2022**, *8*, 475–481. [CrossRef]
3.　Dissanayake, P.D.; Yeom, K.M.; Sarkar, B.; Alessi, D.S.; Hou, D.; Rinklebe, J.; Noh, J.H.; Ok, Y.S. Environmental Impact of Metal Halide Perovskite Solar Cells and Potential Mitigation Strategies: A Critical Review. *Environ. Res.* **2023**, *219*, 115066. [CrossRef] [PubMed]
4.　Mathan Kumar, P.; Das, A.; Seban, L.; Nair, R.G. Fabrication and Life Time of Perovskite Solar Cells. In *Perovskite Photovoltaics Basic to Advanced Concepts and Implementation*; Academic Press: Cambridge, MA, USA, 2018; pp. 231–287. [CrossRef]
5.　Sundaram, S.; Benson, D.; Mallick, T.K. Overview of the PV Industry and Different Technologies. *Sol. Photovolt. Technol. Prod.* **2016**, 7–22. [CrossRef]
6.　Campbell, P.; Green, M.A. High Performance Light Trapping Textures for Monocrystalline Silicon Solar Cells. *Sol. Energy Mater. Sol. Cells* **2001**, *65*, 369–375. [CrossRef]
7.　Khezami, L.; Al Megbel, A.O.; Jemai, A.B.; Ben Rabha, M. Theoretical and Experimental Analysis on Effect of Porous Silicon Surface Treatment in Multicrystalline Silicon Solar Cells. *Appl. Surf. Sci.* **2015**, *353*, 106–111. [CrossRef]
8.　Karyaoui, M.; Bardaoui, A.; Ben Rabha, M.; Harmand, J.C.; Amlouk, M. Effect of Rapid Oxidation on Optical and Electrical Properties of Silicon Nanowires Obtained by Chemical Etching. *EPJ Appl. Phys.* **2012**, *58*, 20103. [CrossRef]
9.　Tan, H.; Santbergen, R.; Smets, A.H.M.; Zeman, M. Plasmonic Light Trapping in Thin-Film Silicon Solar Cells with Improved Self-Assembled Silver Nanoparticles. *Nano Lett.* **2012**, *12*, 4070–4076. [CrossRef]
10.　Wang, Z.; He, J.; Wang, W.; Lin, H.; Xu, Z.; Liu, Q.; Peng, S.; Hou, J.; He, D.; Gao, P. Twenty Percent Efficiency Crystalline Silicon Solar Cells with Solution-Processed Electron-Selective Contacts. *ACS Appl. Energy Mater.* **2021**, *4*, 3644–3650. [CrossRef]
11.　Barkhouse, D.A.R.; Gunawan, O.; Gokmen, T.; Todorov, T.K.; Mitzi, D.B. Yield Predictions for Photovoltaic Power Plants:Empirical Validation,Recent Advances and Remaining Uncertainties. *Prog. Photovolt. Res. Appl.* **2015**, *20*, 6–11. [CrossRef]
12.　Chavan, K.T.; Chandra, S.; Kshirsagar, A. Half-Metallicity in Smallest Cage-like Cluster of CdTe with Doping of Transition Metal Atoms. *Mater. Today Commun.* **2022**, *30*, 103104. [CrossRef]
13.　Chu, T.L.; Chu, S.S. Thin Film II–VI Photovoltaics. *Solid. State. Electron.* **1995**, *38*, 533–549. [CrossRef]
14.　Kumarasinghe, P.K.K.; Dissanayake, A.; Pemasiri, B.M.K.; Dassanayake, B.S. Thermally Evaporated CdTe Thin Films for Solar Cell Applications: Optimization of Physical Properties. *Mater. Res. Bull.* **2017**, *96*, 188–195. [CrossRef]
15.　Rivera, L.P.; García, E.; Cardona, D.; Pérez-Centeno, A.; Camps, E.; Santana-Aranda, M.A.; Gómez-Rosas, G.; de Moure-Flores, F.; Chávez-Chávez, A.; Quiñones-Galván, J.G. CdTe:Sn Thin Films Deposited by the Simultaneous Laser Ablation of CdTe and Sn Targets. *Mater. Res. Express* **2020**, *7*, 015905. [CrossRef]
16.　Camacho-Espinosa, E.; López-Sánchez, A.; Rimmaudo, I.; Mis-Fernández, R.; Peña, J.L. All-Sputtered CdTe Solar Cell Activated with a Novel Method. *Sol. Energy* **2019**, *193*, 31–36. [CrossRef]
17.　Ling, J.; Zhang, X.; Mao, T.; Li, L.; Wang, S.; Cao, M.; Zhang, J.; Shi, H.; Huang, J.; Shen, Y.; et al. Electrodeposition of CdTe Thin Films for Solar Energy Water Splitting. *Materials* **2020**, *13*, 1536. [CrossRef]
18.　Vaishanav, S.K.; Korram, J.; Pradhan, P.; Chandraker, K.; Nagwanshi, R.; Ghosh, K.K.; Satnami, M.L. Green Luminescent CdTe Quantum Dot Based Fluorescence Nano-Sensor for Sensitive Detection of Arsenic (III). *J. Fluoresc.* **2017**, *27*, 781–789. [CrossRef] [PubMed]
19.　Kini, S.; Kulkarni, S.D.; Ganiga, V.; Nagarakshit, T.K.; Chidangil, S. Dual Functionalized, Stable and Water Dispersible CdTe Quantum Dots: Facile, One-Pot Aqueous Synthesis, Optical Tuning and Energy Transfer Applications. *Mater. Res. Bull.* **2019**, *110*, 57–66. [CrossRef]
20.　Duan, J.; Song, L.; Zhan, J. One-Pot Synthesis of Highly Luminescent CdTe Quantum Dots by Microwave Irradiation Reduction and Their Hg^{2+}-Sensitive Properties. *Nano Res.* **2009**, *2*, 61–68. [CrossRef]
21.　Rangel-Cárdenas, J.; Sobral, H. Optical Absorption Enhancement in CdTe Thin Films by Microstructuration of the Silicon Substrate. *Materials* **2017**, *10*, 607. [CrossRef]
22.　Kavanagh, S.R.; Walsh, A.; Scanlon, D.O. Rapid Recombination by Cadmium Vacancies in CdTe. *ACS Energy Lett.* **2021**, *6*, 1392–1398. [CrossRef]
23.　Mendoza-Pérez, R.; Aguilar-Hernández, J.; Sastre-Hernández, J.; Ximello-Quiebras, N.; Contreras-Puente, G.; Santana-Rodríguez, G.; Vigil-Galán, O.; Moreno-García, E.; Morales-Acevedo, A. Photoluminescence Characteristics of CdS Layers Deposited in a Chemical Bath and Their Correlation to CdS/CdTe Solar Cell Performance. *Sol. Energy* **2006**, *80*, 682–686. [CrossRef]
24.　Morales-Acevedo, A. Thin Film CdS/CdTe Solar Cells: Research Perspectives. *Sol. Energy* **2006**, *80*, 675–681. [CrossRef]
25.　O'Regan, B.; Grätzel, M. A Low-Cost, High-Efficiency Solar Cell Based on Dye-Sensitized Colloidal TiO_2 Films. *Nature* **1991**, *353*, 737–740. [CrossRef]

26. Parisi, M.L.; Maranghi, S.; Basosi, R. The Evolution of the Dye Sensitized Solar Cells from Grätzel Prototype to Up-Scaled Solar Applications: A Life Cycle Assessment Approach. *Renew. Sustain. Energy Rev.* **2014**, *39*, 124–138. [CrossRef]

27. Azaid, A.; Raftani, M.; Alaqarbeh, M.; Kacimi, R.; Abram, T.; Khaddam, Y.; Nebbach, D.; Sbai, A.; Lakhlifi, T.; Bouachrine, M. New Organic Dye-Sensitized Solar Cells Based on the D-A-π-A Structure for Efficient DSSCs: DFT/TD-DFT Investigations. *RSC Adv.* **2022**, *12*, 30626–30638. [CrossRef] [PubMed]

28. Lee, C.P.; Li, C.T.; Ho, K.C. Use of Organic Materials in Dye-Sensitized Solar Cells. *Mater. Today* **2017**, *20*, 267–283. [CrossRef]

29. Kwaku Asiam, F.; Mahbubur Rahman, M.; Kumar Kaliamurthy, A.; Muthu, S.; Yadagiri, B.; Cheol Kang, H.; Chen, C.; Yoo, K.; Lee, J.-J. Role of Pi-Electron Density at the Interface of Small Molecule-Sensitized Solar Cells. *J. Phys. Chem. C* **2023**, *127*, 3928–3939. [CrossRef]

30. Soonmin, H.; Hardani; Nandi, P.; Mwankemwa, B.S.; Malevu, T.D.; Malik, M.I. Overview on Different Types of Solar Cells: An Update. *Appl. Sci.* **2023**, *13*, 2051. [CrossRef]

31. Crisp, R.W.; Kirkwood, N.; Grimaldi, G.; Kinge, S.; Siebbeles, L.D.A.; Houtepen, A.J. Highly Photoconductive InP Quantum Dots Films and Solar Cells. *ACS Appl. Energy Mater.* **2018**, *1*, 6569–6576. [CrossRef]

32. Wu, J.; Li, M.-H.; Jiang, Y.; Xu, Q.; Xian, L.; Guo, H.; Wan, J.; Wen, R.; Fang, Y.; Xie, D.; et al. Carrier Management via Integrating InP Quantum Dots into Electron Transport Layer for Efficient Perovskite Solar Cells. *ACS Nano* **2022**, *16*, 15063–15071. [CrossRef]

33. Pidluzhna, A.; Stakhira, P.; Baryshnikov, G.; Zavaraki, A.J.; Ågren, H. InP/ZnS Quantum Dots Synthesis and Photovoltaic Application. *Appl. Nanosci.* **2022**, *13*, 4969–4975. [CrossRef]

34. Halder, G.; Ghosh, D.; Ali, M.Y.; Sahasrabudhe, A.; Bhattacharyya, S. Interface Engineering in Quantum-Dot-Sensitized Solar Cells. *Langmuir* **2018**, *34*, 10197–10216. [CrossRef]

35. Young Kim, J.; Lee, J.-W.; Suk Jung, H.; Shin, H.; Park, N.-G. High-Efficiency Perovskite Solar Cells. *Chem. Rev.* **2020**, *120*, 7867–7918. [CrossRef]

36. Mehrabian, M.; Dalir, S.; Mahmoudi, G.; Miroslaw, B.; Babashkina, M.G.; Dektereva, A.V.; Safin, D.A. A Highly Stable All-Inorganic CsPbBr$_3$ Perovskite Solar Cell. *Eur. J. Inorg. Chem.* **2019**, *2019*, 3699–3703. [CrossRef]

37. Valluvar Oli, A.; Li, Z.; Chen, Y.; Ivaturi, A. Near-Ultraviolet Indoor Black Light-Harvesting Perovskite Solar Cells. *ACS Appl. Energy Mater.* **2022**, *5*, 14669–14679. [CrossRef]

38. Al-Ahmed, A.; Afzaal, M.; Mahar, N.; Khan, F.; Pandey, S.; Zahir, M.H.; Al-Suliman, F.A. The Synergy of Lead Chalcogenide Nanocrystals in Polymeric Bulk Heterojunction Solar Cells. *ACS Omega* **2022**, *7*, 45981–45990. [CrossRef]

39. Tao, S.; Schmidt, I.; Brocks, G.; Jiang, J.; Tranca, I.; Meerholz, K.; Olthof, S. Absolute Energy Level Positions in Tin- and Lead-Based Halide Perovskites. *Nat. Commun.* **2019**, *10*, 2560. [CrossRef] [PubMed]

40. Song, H.; Lin, Y.; Zhou, M.; Rao, H.; Pan, Z.; Zhong, X. Zn-Cu-In-S-Se Quinary "Green" Alloyed Quantum-Dot-Sensitized Solar Cells with a Certified Efficiency of 14.4%. *Angew. Chemie-Int. Ed.* **2021**, *60*, 6137–6144. [CrossRef]

41. Min, H.; Lee, D.Y.; Kim, J.; Kim, G.; Lee, K.S.; Kim, J.; Paik, M.J.; Kim, Y.K.; Kim, K.S.; Kim, M.G.; et al. Perovskite Solar Cells with Atomically Coherent Interlayers on SnO$_2$ Electrodes. *Nature* **2021**, *598*, 444–450. [CrossRef]

42. Park, J.; Kim, J.; Yun, H.-S.; Paik, M.J.; Noh, E.; Mun, H.J.; Kim, M.G.; Shin, T.J.; Seok, S. Il Controlled Growth of Perovskite Layers with Volatile Alkylammonium Chlorides. *Nature* **2023**, *616*, 724–730. [CrossRef]

43. Sulaman, M.; Yang, S.; Imran, A.; Zhang, Z.; Bukhtiar, A.; Ge, Z.; Song, Y.; Sun, F.; Jiang, Y.; Tang, L.; et al. Two Bulk-Heterojunctions Made of Blended Hybrid Nanocomposites for High-Performance Broadband, Self-Driven Photodetectors. *ACS Appl. Mater. Interfaces* **2023**, *15*, 25671–25683. [CrossRef]

44. Sulaman, M.; Yang, S.; Song, Y.; Bukhtiar, A.; Hu, J.; Zhang, Z.; Jiang, Y.; Cui, Y.; Tang, L.; Zou, B. Hybrid Nanocomposites of All-Inorganic Halide Perovskites with Polymers for High-Performance Field-Effect-Transistor-Based Photodetectors: An Experimental and Simulation Study. *Adv. Mater. Interfaces* **2022**, *9*, 2200017. [CrossRef]

45. Sulaman, M.; Yang, S.Y.; Zhang, Z.H.; Imran, A.; Bukhtiar, A.; Ge, Z.H.; Tang, Y.; Jiang, Y.R.; Tang, L.B.; Zou, B.S. Lead-Free Tin-Based Perovskites Nanocrystals for High-Performance Self-Driven Bulk-Heterojunction Photodetectors. *Mater. Today Phys.* **2022**, *27*, 100829. [CrossRef]

46. Sulaman, M.; Yang, S.; Bukhtiar, A.; Tang, P.; Zhang, Z.; Song, Y.; Imran, A.; Jiang, Y.; Cui, Y.; Tang, L.; et al. Hybrid Bulk-Heterojunction of Colloidal Quantum Dots and Mixed-Halide Perovskite Nanocrystals for High-Performance Self-Powered Broadband Photodetectors. *Adv. Funct. Mater.* **2022**, *32*, 2201527. [CrossRef]

47. Dastgeer, G.; Khan, M.F.; Nazir, G.; Afzal, A.M.; Aftab, S.; Naqvi, B.A.; Cha, J.; Min, K.A.; Jamil, Y.; Jung, J.; et al. Temperature-Dependent and Gate-Tunable Rectification in a Black Phosphorus/WS$_2$ van Der Waals Heterojunction Diode. *ACS Appl. Mater. Interfaces* **2018**, *10*, 13150–13157. [CrossRef]

48. Perveen, A.; Hussain, S.; Xu, Y.; Raza, A.; Saeed, F.; Din, N.; Subramanian, A.; Khan, Q.; Lei, W. Solution Processed and Highly Efficient UV-Photodetector Based on CsPbBr$_3$ Perovskite-Polymer Composite Film. *J. Photochem. Photobiol. A Chem.* **2022**, *426*, 113764. [CrossRef]

49. Sulaman, M.; Sulaman, M.; Song, Y.; Yang, S.; Yang, S.; Saleem, M.I.; Li, M.; Perumal Veeramalai, C.; Zhi, R.; Jiang, Y.; et al. Interlayer of PMMA Doped with Au Nanoparticles for High-Performance Tandem Photodetectors: A Solution to Suppress Dark Current and Maintain High Photocurrent. *ACS Appl. Mater. Interfaces* **2020**, *12*, 26153–26160. [CrossRef]

50. Saleem, M.I.; Yang, S.; Zhi, R.; Sulaman, M.; Chandrasekar, P.V.; Jiang, Y.; Tang, Y.; Batool, A.; Zou, B. Surface Engineering of All-Inorganic Perovskite Quantum Dots with Quasi Core–Shell Technique for High-Performance Photodetectors. *Adv. Mater. Interfaces* **2020**, *7*, 2000360. [CrossRef]

51. Saleem, M.I.; Sulaman, M.; Batool, A.; Bukhtiar, A.; Khalid, S. Suppression of Mid-Gap Trap State in CsPbBr$_3$ Nanocrystals with Br-Passivation for Self-Powered Photodetector. *Energy Technol.* **2023**, *11*, 2300013. [CrossRef]

52. Pv-Magazine KAUST Claims 33.2% Efficiency for Perovskite/Silicon Tandem Solar Cell. Available online: https://www.pv-magazine.com/2023/04/13/kaust-claims-33-2-efficiency-for-perovskite-silicon-tandem-solar-cell/ (accessed on 15 June 2023).

53. Lee, W.; Son, H.J.; Lee, D.K.; Kim, B.; Kim, H.; Kim, K.; Ko, M.J. Suppression of Photocorrosion in CdS/CdSe Quantum Dot-Sensitized Solar Cells: Formation of a Thin Polymer Layer on the Photoelectrode Surface. *Synth. Met.* **2013**, *165*, 60–63. [CrossRef]

54. Zhan, L.; Yin, S.; Li, Y.; Li, S.; Chen, T.; Sun, R.; Min, J.; Zhou, G.; Zhu, H.; Chen, Y.; et al. Multiphase Morphology with Enhanced Carrier Lifetime via Quaternary Strategy Enables High-Efficiency, Thick-Film, and Large-Area Organic Photovoltaics. *Adv. Mater.* **2022**, *34*, 2206269. [CrossRef]

55. Zheng, X.; Zuo, L.; Zhao, F.; Li, Y.; Chen, T.; Shan, S.; Yan, K.; Pan, Y.; Xu, B.; Li, C.-Z.; et al. High-Efficiency ITO-Free Organic Photovoltaics with Superior Flexibility and Upscalability. *Adv. Mater.* **2022**, *34*, 2200044. [CrossRef]

56. Zuo, L.; Jo, S.B.; Li, Y.; Meng, Y.; Stoddard, R.J.; Liu, Y.; Lin, F.; Shi, X.; Liu, F.; Hillhouse, H.W. Dilution Effect for Highly Efficient Multiple-Component Organic Solar Cells. *Nat. Nanotechnol.* **2022**, *17*, 53–60. [CrossRef]

57. Kim, T.; Kim, J.-H.; Kang, T.E.; Lee, C.; Kang, H.; Shin, M.; Wang, C.; Ma, B.; Jeong, U.; Kim, T.-S.; et al. Flexible, Highly Efficient All-Polymer Solar Cells. *Nat. Commun.* **2015**, *6*, 8547. [CrossRef]

58. Inganäs, O. Organic Photovoltaics over Three Decades. *Adv. Mater.* **2018**, *30*, 1800388. [CrossRef]

59. Wöhrle, D.; Meissner, D. Organic Solar Cells. *Adv. Mater.* **1991**, *3*, 129–138. [CrossRef]

60. Chamberlain, G.A. Organic Solar Cells: A Review. *Sol. Cells* **1983**, *8*, 47–83. [CrossRef]

61. Yeh, N.; Yeh, P. Organic Solar Cells: Their Developments and Potentials. *Renew. Sustain. Energy Rev.* **2013**, *21*, 421–431. [CrossRef]

62. Morel, D.L.; Ghosh, A.K.; Feng, T.; Stogryn, E.L.; Purwin, P.E.; Shaw, R.F.; Fishman, A.C. High-efficiency Organic Solar Cells. *Appl. Phys. Lett.* **1978**, *32*, 495–497. [CrossRef]

63. Ghosh, A.K.; Feng, T. Merocyanine Organic Solar Cells. *J. Appl. Phys.* **1978**, *49*, 5982–5989. [CrossRef]

64. Tang, C.W. Two-layer Organic Photovoltaic Cell. *Appl. Phys. Lett.* **1986**, *48*, 183–185. [CrossRef]

65. Antoniadis, H.; Hsieh, B.R.; Abkowitz, M.A.; Jenekhe, S.A.; Stolka, M. Photovoltaic and Photoconductive Properties of Aluminum/Poly (p-Phenylene Vinylene) Interfaces. *Synth. Met.* **1994**, *62*, 265–271. [CrossRef]

66. Marks, R.N.; Halls, J.J.M.; Bradley, D.D.C.; Friend, R.H.; Holmes, A.B. The Photovoltaic Response in Poly (p-Phenylene Vinylene) Thin-Film Devices. *J. Phys. Condens. Matter* **1994**, *6*, 1379. [CrossRef]

67. Smilowitz, L.; Sariciftci, N.S.; Wu, R.; Gettinger, C.; Heeger, A.J.; Wudl, F. Photoexcitation Spectroscopy of Conducting-PolymerC$_{60}$ Composites: Photoinduced Electron Transfer. *Phys. Rev. B* **1993**, *47*, 13835–13842. [CrossRef]

68. Sariciftci, N.S.; Smilowitz, L.; Heeger, A.J.; Wudl, F. Photoinduced Electron Transfer from a Conducting Polymer to Buckminsterfullerene. *Science* **1992**, *258*, 1474–1476. [CrossRef]

69. Morita, S.; Kiyomatsu, S.; Yin, X.H.; Zakhidov, A.A.; Noguchi, T.; Ohnishi, T.; Yoshino, K. Doping Effect of Buckminsterfullerene in Poly (2,5-dialkoxy-p-phenylene Vinylene). *J. Appl. Phys.* **1993**, *74*, 2860–2865. [CrossRef]

70. Roman, L.S.; Mammo, W.; Pettersson, L.A.A.; Andersson, M.R.; Inganäs, O. High Quantum Efficiency Polythiophene. *Adv. Mater.* **1998**, *10*, 774–777. [CrossRef]

71. Halls, J.J.M.; Pichler, K.; Friend, R.H.; Moratti, S.C.; Holmes, A.B. Exciton Diffusion and Dissociation in a Poly (P-phenylenevinylene)/C$_{60}$ Heterojunction Photovoltaic Cell. *Appl. Phys. Lett.* **1996**, *68*, 3120–3122. [CrossRef]

72. Yang, C.Y.; Heeger, A.J. Morphology of Composites of Semiconducting Polymers Mixed with C$_{60}$. *Synth. Met.* **1996**, *83*, 85–88. [CrossRef]

73. Yu, G.; Gao, J.; Hummelen, J.C.; Wudl, F.; Heeger, A.J. Polymer Photovoltaic Cells: Enhanced Efficiencies via a Network of Internal Donor-Acceptor Heterojunctions. *Science* **1995**, *270*, 1789–1791. [CrossRef]

74. Gnida, P.; Amin, M.F.; Pajak, A.K.; Jarzabek, B. Polymers in High-Efficiency Solar Cells: The Latest Reports. *Polymers* **2022**, *14*, 1946. [CrossRef]

75. Labiod, A.; Ibraikulov, O.A.; Dabos-Seignon, S.; Ferry, S.; Heinrich, B.; Méry, S.; Fall, S.; Tchognia Nkuissi, H.J.; Heiser, T.; Cabanetos, C.; et al. Photo-Degradation in Bulk Heterojunction Organic Solar Cells Using a Fullerene or a Non-Fullerene Derivative Electron Acceptor. *Org. Electron.* **2022**, *107*, 106549. [CrossRef]

76. Kaim, A.; Piotrowski, P.; Zarębska, K.; Bogdanowicz, K.A.; Przybył, W.; Kwak, A.; Skompska, M.; Gnida, P.; Schab-Balcerzak, E.; Iwan, A. Thermal Imaging and Deep Optical and Electrochemical Study of C$_{70}$ Fullerene Derivatives with Thiophene, Pyrrolidine or Indene Moieties along with Electropolymerization with Thiophene Substituted Imine: Blends with P3HT and PTB7. *Electrochim. Acta* **2022**, *426*, 140741. [CrossRef]

77. Liang, S.; Xiao, C.; Xie, C.; Liu, B.; Fang, H.; Li, W. 13% Single-Component Organic Solar Cells Based on Double-Cable Conjugated Polymers with Pendent Y-Series Acceptors. *Adv. Mater.* **2023**, *35*, e2300629. [CrossRef]

78. Shaheen, S.E.; Brabec, C.J.; Sariciftci, N.S.; Padinger, F.; Fromherz, T.; Hummelen, J.C. 2.5% Efficient Organic Plastic Solar Cells. *Appl. Phys. Lett.* **2001**, *78*, 841–843. [CrossRef]

79. Levitsky, A.; Schneider, S.A.; Rabkin, E.; Toney, M.F.; Frey, G.L. Bridging the Thermodynamics and Kinetics of Temperature-Induced Morphology Evolution in Polymer/Fullerene Organic Solar Cell Bulk Heterojunction. *Mater. Horizons* **2021**, *8*, 1272–1285. [CrossRef]

80. Sprau, C.; Kattenbusch, J.; Li, Y.; Müller, E.; Gerthsen, D.; Berger, R.; Michels, J.J.; Colsmann, A. Revisiting Solvent Additives for the Fabrication of Polymer:Fullerene Solar Cells: Exploring a Series of Benzaldehydes. *Sol. RRL* **2021**, *5*, 2100238. [CrossRef]

81. Grodniski, D.C.; Benatto, L.; Gonçalves, J.P.; de Oliveira, C.C.; Pacheco, K.R.M.; Adad, L.B.; Coturi, V.M.; Roman, L.S.; Koehler, M. High Photothermal Conversion Efficiency for Semiconducting Polymer/Fullerene Nanoparticles and Its Correlation with Photoluminescence Quenching. *RSC Chem. Biol.* **2022**, *4*, 486–503. [CrossRef]

82. Li, S.; Hamada, F.; Nishikubo, R.; Saeki, A. Quantifying the Optimal Thickness in Polymer:Fullerene Solar Cells from the Analysis of Charge Transport Dynamics and Photoabsorption. *Sustain. Energy Fuels* **2022**, *6*, 756–765. [CrossRef]

83. Hoppe, H.; Sariciftci, N.S. Organic Solar Cells: An Overview. *J. Mater. Res.* **2004**, *19*, 1924–1945. [CrossRef]

84. Hou, J.; Inganäs, O.; Friend, R.H.; Gao, F. Organic Solar Cells Based on Non-Fullerene Acceptors. *Nat. Mater.* **2018**, *17*, 119–128. [CrossRef] [PubMed]

85. Kietzke, T. Recent Advances in Organic Solar Cells. *Adv. Optoelectron.* **2007**, *2007*, 40285. [CrossRef]

86. Kim, H.U.; Kim, J.-H.; Kang, H.; Grimsdale, A.C.; Kim, B.J.; Yoon, S.C.; Hwang, D.-H. Naphthalene-, Anthracene-, and Pyrene-Substituted Fullerene Derivatives as Electron Acceptors in Polymer-Based Solar Cells. *ACS Appl. Mater. Interfaces* **2014**, *6*, 20776–20785. [CrossRef] [PubMed]

87. Zhao, G.; He, Y.; Xu, Z.; Hou, J.; Zhang, M.; Min, J.; Chen, H.-Y.; Ye, M.; Hong, Z.; Yang, Y.; et al. Effect of Carbon Chain Length in the Substituent of PCBM-like Molecules on Their Photovoltaic Properties. *Adv. Funct. Mater.* **2010**, *20*, 1480–1487. [CrossRef]

88. Mikroyannidis, J.A.; Kabanakis, A.N.; Sharma, S.S.; Sharma, G.D. A Simple and Effective Modification of PCBM for Use as an Electron Acceptor in Efficient Bulk Heterojunction Solar Cells. *Adv. Funct. Mater.* **2011**, *21*, 746–755. [CrossRef]

89. Xu, X.; Yu, T.; Bi, Z.; Ma, W.; Li, Y.; Peng, Q. Realizing Over 13% Efficiency in Green-Solvent-Processed Nonfullerene Organic Solar Cells Enabled by 1,3,4-Thiadiazole-Based Wide-Bandgap Copolymers. *Adv. Mater.* **2018**, *30*, 1703973. [CrossRef]

90. Lin, Y.; Zhao, F.; He, Q.; Huo, L.; Wu, Y.; Parker, T.C.; Ma, W.; Sun, Y.; Wang, C.; Zhu, D.; et al. High-Performance Electron Acceptor with Thienyl Side Chains for Organic Photovoltaics. *J. Am. Chem. Soc.* **2016**, *138*, 4955–4961. [CrossRef]

91. Li, T.; Dai, S.; Ke, Z.; Yang, L.; Wang, J.; Yan, C.; Ma, W.; Zhan, X. Fused Tris (Thienothiophene)-Based Electron Acceptor with Strong Near-Infrared Absorption for High-Performance As-Cast Solar Cells. *Adv. Mater.* **2018**, *30*, 1705969. [CrossRef]

92. Liu, Q.; Jiang, Y.; Jin, K.; Qin, J.; Xu, J.; Li, W.; Xiong, J.; Liu, J.; Xiao, Z.; Sun, K.; et al. 18% Efficiency Organic Solar Cells. *Sci. Bull.* **2020**, *65*, 272–275. [CrossRef]

93. Zhang, S.; Ye, L.; Hou, J. Breaking the 10% Efficiency Barrier in Organic Photovoltaics: Morphology and Device Optimization of Well-Known PBDTTT Polymers. *Adv. Energy Mater.* **2016**, *6*, 1502529. [CrossRef]

94. Fu, Y.; Lee, T.H.; Chin, Y.-C.; Pacalaj, R.A.; Labanti, C.; Park, S.Y.; Dong, Y.; Cho, H.W.; Kim, J.Y.; Minami, D.; et al. Molecular Orientation-Dependent Energetic Shifts in Solution-Processed Non-Fullerene Acceptors and Their Impact on Organic Photovoltaic Performance. *Nat. Commun.* **2023**, *14*, 1870. [CrossRef]

95. Wang, Y.; Lee, J.; Hou, X.; Labanti, C.; Yan, J.; Mazzolini, E.; Parhar, A.; Nelson, J.; Kim, J.-S.; Li, Z. Recent Progress and Challenges toward Highly Stable Nonfullerene Acceptor-Based Organic Solar Cells. *Adv. Energy Mater.* **2021**, *11*, 2003002. [CrossRef]

96. Lan, W.; Gu, J.; Wu, S.; Peng, Y.; Zhao, M.; Liao, Y.; Xu, T.; Wei, B.; Ding, L.; Zhu, F. Toward Improved Stability of Nonfullerene Organic Solar Cells: Impact of Interlayer and Built-in Potential. *EcoMat* **2021**, *3*, e12134. [CrossRef]

97. Wang, X.; Zhao, C.X.; Xu, G.; Chen, Z.K.; Zhu, F. Degradation Mechanisms in Organic Solar Cells: Localized Moisture Encroachment and Cathode Reaction. *Sol. Energy Mater. Sol. Cells* **2012**, *104*, 1–6. [CrossRef]

98. Fu, J.; Fong, P.W.K.; Liu, H.; Huang, C.-S.; Lu, X.; Lu, S.; Abdelsamie, M.; Kodalle, T.; Sutter-Fella, C.M.; Yang, Y.; et al. 19.31% Binary Organic Solar Cell and Low Non-Radiative Recombination Enabled by Non-Monotonic Intermediate State Transition. *Nat. Commun.* **2023**, *14*, 1760. [CrossRef]

99. Tarique, W.B.; Uddin, A. A Review of Progress and Challenges in the Research Developments on Organic Solar Cells. *Mater. Sci. Semicond. Process.* **2023**, *163*, 107541. [CrossRef]

100. Adnan, M.; Irshad, Z.; Hussain, R.; Lee, W.; Kim, M.; Lim, J. Efficient Ternary Active Layer Materials for Organic Photovoltaics. *Sol. Energy* **2023**, *257*, 324–343. [CrossRef]

101. Li, D.; Deng, N.; Fu, Y.; Guo, C.; Zhou, B.; Wang, L.; Zhou, J.; Liu, D.; Li, W.; Wang, K.; et al. Fibrillization of Non-Fullerene Acceptors Enables 19% Efficiency Pseudo-Bulk Heterojunction Organic Solar Cells. *Adv. Mater.* **2023**, *35*, 2208211. [CrossRef]

102. Zhang, Y.; Lang, Y.; Li, G. Recent Advances of Non-Fullerene Organic Solar Cells: From Materials and Morphology to Devices and Applications. *EcoMat* **2023**, *5*, e12281. [CrossRef]

103. Gu, X.; Lai, X.; Zhang, Y.; Wang, T.; Tan, W.L.; McNeill, C.R.; Liu, Q.; Sonar, P.; He, F.; Li, W.; et al. Organic Solar Cell With Efficiency Over 20% and VOC Exceeding 2.1 V Enabled by Tandem with All-Inorganic Perovskite and Thermal Annealing-Free Process. *Adv. Sci.* **2022**, *9*, e2200445. [CrossRef] [PubMed]

104. Zhu, L.; Zhang, M.; Xu, J.; Li, C.; Yan, J.; Zhou, G.; Zhong, W.; Hao, T.; Song, J.; Xue, X.; et al. Single-Junction Organic Solar Cells with over 19% Efficiency Enabled by a Refined Double-Fibril Network Morphology. *Nat. Mater.* **2022**, *21*, 656–663. [CrossRef]

105. Cui, Y.; Xu, Y.; Yao, H.; Bi, P.; Hong, L.; Zhang, J.; Zu, Y.; Zhang, T.; Qin, J.; Ren, J.; et al. Single-Junction Organic Photovoltaic Cell with 19% Efficiency. *Adv. Mater.* **2021**, *33*, 2102420. [CrossRef]

106. Green, M.A.; Dunlop, E.D.; Siefer, G.; Yoshita, M.; Kopidakis, N.; Bothe, K.; Hao, X. Solar Cell Efficiency Tables (Version 61). *Prog. Photovolt. Res. Appl.* **2023**, *31*, 3–16. [CrossRef]

107. Ding, G.; Chen, T.; Wang, M.; Xia, X.; He, C.; Zheng, X.; Li, Y.; Zhou, D.; Lu, X.; Zuo, L.; et al. Solid Additive-Assisted Layer-by-Layer Processing for 19% Efficiency Binary Organic Solar Cells. *Nano-Micro Lett.* **2023**, *15*, 92. [CrossRef]

108. Balakirev, D.O.; Mannanov, A.L.; Emelianov, N.A.; Sukhorukova, P.K.; Kalinichenko, A.K.; Troshin, P.A.; Paraschuk, D.Y.; Ponomarenko, S.A.; Luponosov, Y.N. Star-Shaped Benzotriindole-Based Donor Compounds for All–Small–Molecule Non-Fullerene Organic Solar Cells. *Dye. Pigment.* **2023**, *216*, 111343. [CrossRef]
109. Shi, Y.; Zhu, L.; Yan, Y.; Xie, M.; Liang, G.; Qiao, J.; Zhang, J.; Hao, X.; Lu, K.; Wei, Z. Small Energetic Disorder Enables Ultralow Energy Losses in Non-Fullerene Organic Solar Cells. *Adv. Energy Mater.* **2023**, *13*, 2300458. [CrossRef]
110. Zhan, L.; Li, S.; Zhang, S.; Chen, X.; Lau, T.-K.; Lu, X.; Shi, M.; Li, C.-Z.; Chen, H. Enhanced Charge Transfer between Fullerene and Non-Fullerene Acceptors Enables Highly Efficient Ternary Organic Solar Cells. *ACS Appl. Mater. Interfaces* **2018**, *10*, 42444–42452. [CrossRef]
111. Hai, J.; Song, Y.; Li, L.; Liu, X.; Shi, X.; Huang, Z.; Qian, G.; Lu, Z.; Yu, J.; Hu, H.; et al. High-Efficiency Organic Solar Cells Enabled by Chalcogen Containing Branched Chain Engineering: Balancing Short-Circuit Current and Open-Circuit Voltage, Enhancing Fill Factor. *Adv. Funct. Mater.* **2023**, *33*, 2213429. [CrossRef]
112. Xu, X.; Jing, W.; Meng, H.; Guo, Y.; Yu, L.; Li, R.; Peng, Q. Sequential Deposition of Multicomponent Bulk Heterojunctions Increases Efficiency of Organic Solar Cells. *Adv. Mater.* **2023**, *35*, e2208997. [CrossRef]
113. Zhang, G.; Chen, Q.; Zhang, Z.; Fang, J.; Zhao, C.; Wei, Y.; Li, W. Co-La-Based Hole-Transporting Layers for Binary Organic Solar Cells with 18.82% Efficiency. *Angew. Chemie-Int. Ed.* **2023**, *62*, e202216304. [CrossRef]
114. Cheng, P.; Li, G.; Zhan, X.; Yang, Y. Next-Generation Organic Photovoltaics Based on Non-Fullerene Acceptors. *Nat. Photonics* **2018**, *12*, 131–142. [CrossRef]
115. Rafique, S.; Abdullah, S.M.; Sulaiman, K.; Iwamoto, M. Fundamentals of Bulk Heterojunction Organic Solar Cells: An Overview of Stability/Degradation Issues and Strategies for Improvement. *Renew. Sustain. Energy Rev.* **2018**, *84*, 43–53. [CrossRef]
116. Halls, J.J.M.; Walsh, C.A.; Greenham, N.C.; Marseglia, E.A.; Friend, R.H.; Moratti, S.C.; Holmes, A.B. Efficient Photodiodes from Interpenetrating Polymer Networks. *Nature* **1995**, *376*, 498–500. [CrossRef]
117. He, C.; Bi, Z.; Chen, Z.; Guo, J.; Xia, X.; Lu, X.; Min, J.; Zhu, H.; Ma, W.; Zuo, L.; et al. Compromising Charge Generation and Recombination with Asymmetric Molecule for High-Performance Binary Organic Photovoltaics with over 18% Certified Efficiency. *Adv. Funct. Mater.* **2022**, *32*, 2112511. [CrossRef]
118. Yao, J.; Ding, S.; Zhang, R.; Bai, Y.; Zhou, Q.; Meng, L.; Solano, E.; Steele, J.A.; Roeffaers, M.B.J.; Gao, F.; et al. Fluorinated Perylene-Diimides: Cathode Interlayers Facilitating Carrier Collection for High-Performance Organic Solar Cells. *Adv. Mater.* **2022**, *34*, 2203690. [CrossRef]
119. Heeger, A.J. 25th Anniversary Article: Bulk Heterojunction Solar Cells: Understanding the Mechanism of Operation. *Adv. Mater.* **2014**, *26*, 10–28. [CrossRef]
120. Wang, Z.; Gao, K.; Kan, Y.; Zhang, M.; Qiu, C.; Zhu, L.; Zhao, Z.; Peng, X.; Feng, W.; Qian, Z.; et al. The Coupling and Competition of Crystallization and Phase Separation, Correlating Thermodynamics and Kinetics in OPV Morphology and Performances. *Nat. Commun.* **2021**, *12*, 332. [CrossRef]
121. Dey, S. Recent Progress in Molecular Design of Fused Ring Electron Acceptors for Organic Solar Cells. *Small* **2019**, *15*, 1900134. [CrossRef]
122. Fu, H.; Wang, Z.; Sun, Y. Advances in Non-Fullerene Acceptor Based Ternary Organic Solar Cells. *Sol. RRL* **2018**, *2*, 1700158. [CrossRef]
123. Zhang, J.; Zhang, Y.; Fang, J.; Lu, K.; Wang, Z.; Ma, W.; Wei, Z. Conjugated Polymer–Small Molecule Alloy Leads to High Efficient Ternary Organic Solar Cells. *J. Am. Chem. Soc.* **2015**, *137*, 8176–8183. [CrossRef]
124. Cheng, P.; Li, Y.; Zhan, X. Efficient Ternary Blend Polymer Solar Cells with Indene-C$_{60}$ Bisadduct as an Electron-Cascade Acceptor. *Energy Environ. Sci.* **2014**, *7*, 2005–2011. [CrossRef]
125. Lu, L.; Chen, W.; Xu, T.; Yu, L. High-Performance Ternary Blend Polymer Solar Cells Involving both Energy Transfer and Hole Relay Processes. *Nat. Commun.* **2015**, *6*, 7327. [CrossRef] [PubMed]
126. Liu, B.; Sun, H.; Lee, J.-W.; Jiang, Z.; Qiao, J.; Wang, J.; Yang, J.; Feng, K.; Liao, Q.; An, M.; et al. Efficient and Stable Organic Solar Cells Enabled by Multicomponent Photoactive Layer Based on One-Pot Polymerization. *Nat. Commun.* **2023**, *14*, 967. [CrossRef]
127. Yu, H.; Wang, Y.; Zou, X.; Yin, J.; Shi, X.; Li, Y.; Zhao, H.; Wang, L.; Ng, H.M.; Zou, B.; et al. Improved Photovoltaic Performance and Robustness of All-Polymer Solar Cells Enabled by a Polyfullerene Guest Acceptor. *Nat. Commun.* **2023**, *14*, 2323. [CrossRef] [PubMed]
128. Liu, Z.; Wang, L.; Zhao, H.; Chen, P.; Xie, X. High-Performance Inverted Ternary Organic Solar Cells Using Solution-Processed Tin Oxide as the Electron Transport Layer. *Org. Electron.* **2023**, *120*, 106828. [CrossRef]
129. Liu, M.; Ge, X.; Jiang, X.; Chen, D.; Guo, F.; Gao, S.; Peng, Q.; Zhao, L.; Zhang, Y. 18% Efficiency of Ternary Organic Solar Cells Enabled by Integrating a Fused Perylene Diimide Guest Acceptor. *Nano Energy* **2023**, *112*, 108501. [CrossRef]
130. Lv, J.; Yang, Q.; Deng, W.; Chen, H.; Kumar, M.; Zhao, F.; Lu, S.; Hu, H.; Kan, Z. Isomeric Acceptors Incorporation Enables 18.1% Efficiency Ternary Organic Solar Cells with Reduced Trap-Assisted Charge Recombination. *Chem. Eng. J.* **2023**, *465*, 142822. [CrossRef]
131. Xu, R.; Jiang, Y.; Liu, F.; Su, W.; Liu, W.; Xu, S.; Fan, H.; Jiang, C.; Zong, Q.; Zhang, W.; et al. Efficient Ternary Organic Solar Cells Enabled by Asymmetric Nonfullerene Electron Acceptor with Suppressed Nonradiative Recombination. *Chem. Eng. J.* **2023**, *464*, 142507. [CrossRef]
132. Ram, K.S.; Singh, J. Over 20% Efficient and Stable Non-Fullerene-Based Ternary Bulk-Heterojunction Organic Solar Cell with WS2 Hole-Transport Layer and Graded Refractive Index Antireflection Coating. *Adv. Theory Simul.* **2020**, *3*, 2000047. [CrossRef]

133. Bi, P.; Wang, J.; Cui, Y.; Zhang, J.; Zhang, T.; Chen, Z.; Qiao, J.; Dai, J.; Zhang, S.; Hao, X. Enhancing Photon Utilization Efficiency for High-Performance Organic Photovoltaic Cells via Regulating Phase-Transition Kinetics. *Adv. Mater.* **2023**, *35*, e2210865. [CrossRef]

134. Jia, Z.; Qin, S.; Meng, L.; Ma, Q.; Angunawela, I.; Zhang, J.; Li, X.; He, Y.; Lai, W.; Li, N.; et al. High Performance Tandem Organic Solar Cells via a Strongly Infrared-Absorbing Narrow Bandgap Acceptor. *Nat. Commun.* **2021**, *12*, 178. [CrossRef] [PubMed]

135. Lu, S.; Ouyang, D.; Choy, W.C.H. Recent Progress of Interconnecting Layer for Tandem Organic Solar Cells. *Sci. China Chem.* **2017**, *60*, 460–471. [CrossRef]

136. Guo, B.; Li, W.; Luo, G.; Guo, X.; Yao, H.; Zhang, M.; Hou, J.; Li, Y.; Wong, W.-Y. Exceeding 14% Efficiency for Solution-Processed Tandem Organic Solar Cells Combining Fullerene-and Nonfullerene-Based Subcells with Complementary Absorption. *ACS Energy Lett.* **2018**, *3*, 2566–2572. [CrossRef]

137. Li, Y.; Huang, W.; Zhao, D.; Wang, L.; Jiao, Z.; Huang, Q.; Wang, P.; Sun, M.; Yuan, G. Recent Progress in Organic Solar Cells: A Review on Materials from Acceptor to Donor. *Molecules* **2022**, *27*, 1800. [CrossRef] [PubMed]

138. Almuqoddas, E.; Neophytou, M.; Widianto, E.; Nursam, N.M.; Shobih; Pranoto, L.M.; Firdaus, Y. Semi-Transparent Fullerene-Based Tandem Solar Cells with Excellent Light Utilization Efficiency Enabled by Careful Selection of Sub-Cells. *Org. Electron.* **2022**, *109*, 106633. [CrossRef]

139. Meng, L.; Zhang, Y.; Wan, X.; Li, C.; Zhang, X.; Wang, Y.; Ke, X.; Xiao, Z.; Ding, L.; Xia, R.; et al. Organic and Solution-Processed Tandem Solar Cells with 17.3% Efficiency. *Science* **2018**, *361*, 1094–1098. [CrossRef]

140. Liu, G.; Xia, R.; Huang, Q.; Zhang, K.; Hu, Z.; Jia, T.; Liu, X.; Yip, H.-L.; Huang, F. Tandem Organic Solar Cells with 18.7% Efficiency Enabled by Suppressing the Charge Recombination in Front Sub-Cell. *Adv. Funct. Mater.* **2021**, *31*, 2103283. [CrossRef]

141. Zheng, Z.; Wang, J.; Bi, P.; Ren, J.; Wang, Y.; Yang, Y.; Liu, X.; Zhang, S.; Hou, J. Tandem Organic Solar Cell with 20.2% Efficiency. *Joule* **2022**, *6*, 171–184. [CrossRef]

142. Grätzel, M. Photoelectrochemical Cells. *Nature* **2001**, *414*, 338–344. [CrossRef]

143. Kalyanasundaram, K.; Grätzel, M. Applications of Functionalized Transition Metal Complexes in Photonic and Optoelectronic Devices. *Coord. Chem. Rev.* **1998**, *177*, 347–414. [CrossRef]

144. Grätzel, M. Dye-Sensitized Solar Cells. *J. Photochem. Photobiol. C Photochem. Rev.* **2003**, *4*, 145–153. [CrossRef]

145. Grobelny, A.; Shen, Z.; Eickemeyer, F.T.; Antariksa, N.F.; Zapotoczny, S.; Zakeeruddin, S.M.; Grätzel, M. A Molecularly Tailored Photosensitizer with an Efficiency of 13.2% for Dye-Sensitized Solar Cells. *Adv. Mater.* **2023**, *35*, 2207785. [CrossRef] [PubMed]

146. Ren, Y.; Cao, Y.; Zhang, D.; Zakeeruddin, S.M.; Hagfeldt, A.; Wang, P.; Grätzel, M. A Blue Photosensitizer Realizing Efficient and Stable Green Solar Cells via Color Tuning by the Electrolyte. *Adv. Mater.* **2020**, *32*, 2000193. [CrossRef]

147. Dou, J.; Chen, Q. MOFs in Emerging Solar Cells. *Chin. J. Chem.* **2023**, *41*, 695–709. [CrossRef]

148. Bandara, T.M.W.J.; Hansadi, J.M.C.; Bella, F. A Review of Textile Dye-Sensitized Solar Cells for Wearable Electronics. *Ionics* **2022**, *28*, 2563–2583. [CrossRef]

149. Devadiga, D.; Selvakumar, M.; Shetty, P.; Santosh, M.S. The Integration of Flexible Dye-Sensitized Solar Cells and Storage Devices towards Wearable Self-Charging Power Systems: A Review. *Renew. Sustain. Energy Rev.* **2022**, *159*, 112252. [CrossRef]

150. Barbato, M.; Artegiani, E.; Bertoncello, M.; Meneghini, M.; Ortolani, L.; Zanoni, E.; Meneghesso, G. CdTe Solar Cells: Technology, Operation and Reliability. *J. Phys. D Appl. Phys.* **2021**, *54*, 333002. [CrossRef]

151. Sameera, J.N.; Islam, M.A.; Islam, S.; Hossain, T.; Sobayel, M.K.; Akhtaruzzaman, M.; Amin, N.; Rashid, M.J. Cubic Silicon Carbide (3C–SiC) as a Buffer Layer for High Efficiency and Highly Stable CdTe Solar Cell. *Opt. Mater.* **2022**, *123*, 111911. [CrossRef]

152. Buitrago, E.; Novello, A.M.; Meyer, T. Third-Generation Solar Cells: Toxicity and Risk of Exposure. *Helv. Chim. Acta* **2020**, *103*, e2000074. [CrossRef]

153. Rimmaudo, I.; Salavei, A.; Artegiani, E.; Menossi, D.; Giarola, M.; Mariotto, G.; Gasparotto, A.; Romeo, A. Improved Stability of CdTe Solar Cells by Absorber Surface Etching. *Sol. Energy Mater. Sol. Cells* **2017**, *162*, 127–133. [CrossRef]

154. Zhang, H.; Cheng, K.; Hou, Y.M.; Fang, Z.; Pan, Z.X.; Wu, W.J.; Hua, J.L.; Zhong, X.H. Efficient CdSe Quantum Dot-Sensitized Solar Cells Prepared by a Postsynthesis Assembly Approach. *Chem. Commun.* **2012**, *48*, 11235–11237. [CrossRef] [PubMed]

155. Zheng, S.; Chen, J.; Johansson, E.M.J.; Zhang, X. PbS Colloidal Quantum Dot Inks for Infrared Solar Cells. *iScience* **2020**, *23*, 101753. [CrossRef]

156. Sun, B.; Johnston, A.; Xu, C.; Wei, M.; Huang, Z.; Jiang, Z.; Zhou, H.; Gao, Y.; Dong, Y.; Ouellette, O.; et al. Monolayer Perovskite Bridges Enable Strong Quantum Dot Coupling for Efficient Solar Cells. *Joule* **2020**, *4*, 1542–1556. [CrossRef]

157. Aldakov, D.; Lefrançois, A.; Reiss, P. Ternary and Quaternary Metal Chalcogenide Nanocrystals: Synthesis, Properties and Applications. *J. Mater. Chem.C* **2013**, *1*, 3756–3776. [CrossRef]

158. Ramanujam, J.; Singh, U.P. Copper Indium Gallium Selenide Based Solar Cells—A Review. *Energy Environ. Sci.* **2017**, *10*, 1306–1319. [CrossRef]

159. Belghachi, A.; Limam, N. Effect of the Absorber Layer Band-Gap on CIGS Solar Cell. *Chin. J. Phys.* **2017**, *55*, 1127–1134. [CrossRef]

160. Bouich, A.; Ullah, S.; Ullah, H.; Mari, B.; Hartiti, B.; Ebn Touhami, M.; Santos, D.M.F. Deposit on Different Back Contacts: To High-Quality CuInGaS2 Thin Films for Photovoltaic Application. *J. Mater. Sci. Mater. Electron.* **2019**, *30*, 20832–20839. [CrossRef]

161. Stuckelberger, M.E.; Nietzold, T.; West, B.M.; Farshchi, R.; Poplavskyy, D.; Bailey, J.; Lai, B.; Maser, J.M.; Bertoni, M.I. How Does CIGS Performance Depend on Temperature at the Microscale? *IEEE J. Photovoltaics* **2018**, *8*, 278–287. [CrossRef]

162. Vaillon, R.; Parola, S.; Lamnatou, C.; Chemisana, D. Solar Cells Operating under Thermal Stress. *Cell Reports Phys. Sci.* **2020**, *1*, 100267. [CrossRef]

163. Nakamura, M.; Yamaguchi, K.; Kimoto, Y.; Yasaki, Y.; Kato, T.; Sugimoto, H. Cd-Free Cu(In,Ga)(Se,S)$_2$ Thin-Film Solar Cell with Record Efficiency of 23.35%. *IEEE J. Photovoltaics* **2019**, *9*, 1863–1867. [CrossRef]

164. Kwak, J.I.; Nam, S.H.; Kim, L.; An, Y.J. Potential Environmental Risk of Solar Cells: Current Knowledge and Future Challenges. *J. Hazard. Mater.* **2020**, *392*, 122297. [CrossRef]

165. Nakamura, M.; Tada, K.; Kinoshita, T.; Bessho, T.; Nishiyama, C.; Takenaka, I.; Kimoto, Y.; Higashino, Y.; Sugimoto, H.; Segawa, H. Perovskite/CIGS Spectral Splitting Double Junction Solar Cell with 28% Power Conversion Efficiency. *iScience* **2020**, *23*, 101817. [CrossRef] [PubMed]

166. Theelen, M.; Foster, C.; Steijvers, H.; Barreau, N.; Vroon, Z.; Zeman, M. The Impact of Atmospheric Species on the Degradation of CIGS Solar Cells. *Sol. Energy Mater. Sol. Cells* **2015**, *141*, 49–56. [CrossRef]

167. Ito, K. (Ed.) *Copper Zinc Tin Sulfide-Based Thin Film Solar Cells*, 1st ed.; John Wiley and Sons Ltd.: Hoboken, NJ, USA, 2015; ISBN 9781118437872.

168. Sravani, L.; Routray, S.; Pradhan, K.P.; Piedrahita, M.C. Kesterite Thin-Film Solar Cell: Role of Grain Boundaries and Defects in Copper–Zinc–Tin–Sulfide and Copper–Zinc–Tin–Selenide. *Phys. Status Solidi Appl. Mater. Sci.* **2021**, *218*, 2100039. [CrossRef]

169. Sun, K.; Yan, C.; Liu, F.; Huang, J.; Zhou, F.; Stride, J.A.; Green, M.; Hao, X. Over 9% Efficient Kesterite Cu$_2$ZnSnS$_4$ Solar Cell Fabricated by Using Zn$_{1−x}$Cd$_x$S Buffer Layer. *Adv. Energy Mater.* **2016**, *6*, 4–9. [CrossRef]

170. Pal, K.; Singh, P.; Bhaduri, A.; Thapa, K.B. Current Challenges and Future Prospects for a Highly Efficient (>20%) Kesterite CZTS Solar Cell: A Review. *Sol. Energy Mater. Sol. Cells* **2019**, *196*, 138–156. [CrossRef]

171. Wei, Y.; Zhuang, D.; Zhao, M.; Gong, Q.; Sun, R.; Ren, G.; Wu, Y.; Zhang, L.; Lyu, X.; Peng, X.; et al. An Investigation on the Relationship between Open Circuit Voltage and Grain Size for CZTSSe Thin Film Solar Cells Fabricated by Selenization of Sputtered Precursors. *J. Alloys Compd.* **2019**, *773*, 689–697. [CrossRef]

172. Li, J.; Huang, Y.; Huang, J.; Liang, G.; Zhang, Y.; Rey, G.; Guo, F.; Su, Z.; Zhu, H.; Cai, L.; et al. Defect Control for 12.5% Efficiency Cu2ZnSnSe4 Kesterite Thin-Film Solar Cells by Engineering of Local Chemical Environment. *Adv. Mater.* **2020**, *32*, e2005268. [CrossRef] [PubMed]

173. Dwivedi, S.K.; Tripathi, S.K.; Tiwari, D.C.; Chauhan, A.S.; Dwivedi, P.K.; Eswara Prasad, N. Low Cost Copper Zinc Tin Sulphide (CZTS) Solar Cells Fabricated by Sulphurizing Sol-Gel Deposited Precursor Using 1,2-Ethanedithiol (EDT). *Sol. Energy* **2021**, *224*, 210–217. [CrossRef]

174. Liu, Y.; Hu, C.; Qi, Y.; Zhou, W.; Kou, D.; Zhou, Z.; Han, L.; Meng, Y.; Yuan, S.; Wu, S. Li/Ag Co-Doping Synergistically Boosts the Efficiency of Kesterite Solar Cells Through Effective SnZn Defect Passivation. *Adv. Mater. Interfaces* **2022**, *9*, 2201677. [CrossRef]

175. Romeo, A.; Artegiani, E. CdTe-Based Thin Film Solar Cells: Past, Present and Future. *Energies* **2021**, *14*, 1684. [CrossRef]

176. Ward, J.S.; Ramanathan, K.; Hasoon, F.S.; Coutts, T.J.; Keane, J.; Contreras, M.A.; Moriarty, T.; Noufi, R. A 21·5% Efficient Cu(In,Ga)Se2 Thin-Film Concentrator Solar Cell. *Prog. Photovolt. Res. Appl.* **2002**, *10*, 41–46. [CrossRef]

177. Yan, C.; Huang, J.; Sun, K.; Johnston, S.; Zhang, Y.; Sun, H.; Pu, A.; He, M.; Liu, F.; Eder, K.; et al. Cu$_2$ZnSnS$_4$ Solar Cells with over 10% Power Conversion Efficiency Enabled by Heterojunction Heat Treatment. *Nat. Energy* **2018**, *3*, 764–772. [CrossRef]

178. Giraldo, S.; Saucedo, E.; Neuschitzer, M.; Oliva, F.; Placidi, M.; Alcobé, X.; Izquierdo-Roca, V.; Kim, S.; Tampo, H.; Shibata, H.; et al. How Small Amounts of Ge Modify the Formation Pathways and Crystallization of Kesterites. *Energy Environ. Sci.* **2018**, *11*, 582–593. [CrossRef]

179. Wang, W.; Winkler, M.T.; Gunawan, O.; Gokmen, T.; Todorov, T.K.; Zhu, Y.; Mitzi, D.B. Device Characteristics of CZTSSe Thin-Film Solar Cells with 12.6% Efficiency. *Adv. Energy Mater.* **2014**, *4*, 1301465. [CrossRef]

180. Moon, S.H.; Park, S.J.; Kim, S.H.; Lee, M.W.; Han, J.; Kim, J.Y.; Kim, H.; Hwang, Y.J.; Lee, D.K.; Min, B.K. Monolithic DSSC/CIGS Tandem Solar Cell Fabricated by a Solution Process. *Sci. Rep.* **2015**, *5*, srep08970. [CrossRef]

181. Hadipour, A.; de Boer, B.; Blom, P.W.M. Device Operation of Organic Tandem Solar Cells. *Org. Electron.* **2008**, *9*, 617–624. [CrossRef]

182. Enam, F.M.T.; Rahman, K.S.; Kamaruzzaman, M.I.; Sobayel, K.; Chelvanathan, P.; Bais, B.; Akhtaruzzaman, M.; Alamoud, A.R.M.; Amin, N. Design Prospects of Cadmium Telluride/Silicon (CdTe/Si) Tandem Solar Cells from Numerical Simulation. *Optik* **2017**, *139*, 397–406. [CrossRef]

183. Hosokawa, H.; Tamaki, R.; Sawada, T.; Okonogi, A.; Sato, H.; Ogomi, Y.; Hayase, S.; Okada, Y.; Yano, T. Solution-Processed Intermediate-Band Solar Cells with Lead Sulfide Quantum Dots and Lead Halide Perovskites. *Nat. Commun.* **2019**, *10*, 4–6. [CrossRef]

184. Andruszkiewicz, A.; Zhang, X.; Johansson, M.B.; Yuan, L.; Johansson, E.M.J. Perovskite and Quantum Dot Tandem Solar Cells with Interlayer Modification for Improved Optical Semitransparency and Stability. *Nanoscale* **2021**, *13*, 6234–6240. [CrossRef]

185. Todorov, T.; Gershon, T.; Gunawan, O.; Sturdevant, C.; Guha, S. Perovskite-Kesterite Monolithic Tandem Solar Cells with High Open-Circuit Voltage. *Appl. Phys. Lett.* **2014**, *105*, 173902. [CrossRef]

186. Saha, U.; Alam, M.K. Proposition and Computational Analysis of a Kesterite/Kesterite Tandem Solar Cell with Enhanced Efficiency. *RSC Adv.* **2017**, *7*, 4806–4814. [CrossRef]

187. Song, Z.; Chen, C.; Li, C.; Awni, R.A.; Zhao, D.; Yan, Y. Wide-Bandgap, Low-Bandgap, and Tandem Perovskite Solar Cells. *Semicond. Sci. Technol.* **2019**, *34*, 093001. [CrossRef]

188. Gu, S.; Lin, R.; Han, Q.; Gao, Y.; Tan, H.; Zhu, J. Tin and Mixed Lead–Tin Halide Perovskite Solar Cells: Progress and Their Application in Tandem Solar Cells. *Adv. Mater.* **2020**, *32*, e1907392. [CrossRef] [PubMed]

189. Wang, R.; Huang, T.; Xue, J.; Tong, J.; Zhu, K.; Yang, Y. Prospects for Metal Halide Perovskite-Based Tandem Solar Cells. *Nat. Photonics* **2021**, *15*, 411–425. [CrossRef]

190. Fang, Z.; Zeng, Q.; Zuo, C.; Zhang, L.; Xiao, H.; Cheng, M.; Hao, F.; Bao, Q.; Zhang, L.; Yuan, Y.; et al. Perovskite-Based Tandem Solar Cells. *Sci. Bull.* **2021**, *66*, 621–636. [CrossRef]

191. Shen, H.; Duong, T.; Peng, J.; Jacobs, D.; Wu, N.; Gong, J.; Wu, Y.; Karuturi, S.K.; Fu, X.; Weber, K.; et al. Mechanically-Stacked Perovskite/CIGS Tandem Solar Cells with Efficiency of 23.9% and Reduced Oxygen Sensitivity. *Energy Environ. Sci.* **2018**, *11*, 394–406. [CrossRef]

192. Li, H.; Zhang, W. Perovskite Tandem Solar Cells: From Fundamentals to Commercial Deployment. *Chem. Rev.* **2020**, *120*, 9835–9950. [CrossRef] [PubMed]

193. Al-Ashouri, A.; Magomedov, A.; Roß, M.; Jošt, M.; Talaikis, M.; Chistiakova, G.; Bertram, T.; Márquez, J.A.; Köhnen, E.; Kasparavičius, E.; et al. Conformal Monolayer Contacts with Lossless Interfaces for Perovskite Single Junction and Monolithic Tandem Solar Cells. *Energy Environ. Sci.* **2019**, *12*, 3356–3369. [CrossRef]

194. Jošt, M.; Köhnen, E.; Al-Ashouri, A.; Bertram, T.; Tomšič, Š.; Magomedov, A.; Kasparavicius, E.; Kodalle, T.; Lipovšek, B.; Getautis, V.; et al. Perovskite/CIGS Tandem Solar Cells: From Certified 24.2% toward 30% and Beyond. *ACS Energy Lett.* **2022**, *7*, 1298–1307. [CrossRef]

195. Manekkathodi, A.; Chen, B.; Kim, J.; Baek, S.W.; Scheffel, B.; Hou, Y.; Ouellette, O.; Saidaminov, M.I.; Voznyy, O.; Madhavan, V.E.; et al. Solution-Processed Perovskite-Colloidal Quantum Dot Tandem Solar Cells for Photon Collection beyond 1000 Nm. *J. Mater. Chem. A* **2019**, *7*, 26020–26028. [CrossRef]

196. Xiao, K.; Lin, R.; Han, Q.; Hou, Y.; Qin, Z.; Nguyen, H.T.; Wen, J.; Wei, M.; Yeddu, V.; Saidaminov, M.I.; et al. All-Perovskite Tandem Solar Cells with 24.2% Certified Efficiency and Area over 1 cm^2 Using Surface-Anchoring Zwitterionic Antioxidant. *Nat. Energy* **2020**, *5*, 870–880. [CrossRef]

197. Jang, Y.H.; Lee, J.M.; Seo, J.W.; Kim, I.; Lee, D.K. Monolithic Tandem Solar Cells Comprising Electrodeposited CuInSe$_2$ and Perovskite Solar Cells with a Nanoparticulate ZnO Buffer Layer. *J. Mater. Chem. A* **2017**, *5*, 19439–19446. [CrossRef]

198. Madan, J.; Singh, K.; Pandey, R. Comprehensive Device Simulation of 23.36% Efficient Two-Terminal Perovskite-PbS CQD Tandem Solar Cell for Low-Cost Applications. *Sci. Rep.* **2021**, *11*, 19829. [CrossRef] [PubMed]

199. Makita, K.; Kamikawa, Y.; Mizuno, H.; Oshima, R.; Shoji, Y.; Ishizuka, S.; Müller, R.; Beutel, P.; Lackner, D.; Benick, J.; et al. III-V//Cu$_x$In$_{1-y}$Ga$_y$Se$_2$ Multijunction Solar Cells with 27.2% Efficiency Fabricated Using Modified Smart Stack Technology with Pd Nanoparticle Array and Adhesive Material. *Prog. Photovolt. Res. Appl.* **2021**, *29*, 887–898. [CrossRef]

200. Grassman, T.J.; Chmielewski, D.J.; Carnevale, S.D.; Carlin, J.A.; Ringel, S.A. GaAs$_{0.75}$P$_{0.25}$/Si Dual-Junction Solar Cells Grown by MBE and MOCVD. *IEEE J. Photovolt.* **2016**, *6*, 326–331. [CrossRef]

201. Greenaway, A.L.; Loutris, A.L.; Heinselman, K.N.; Melamed, C.L.; Schnepf, R.R.; Tellekamp, M.B.; Woods-Robinson, R.; Sherbondy, R.; Bardgett, D.; Bauers, S.; et al. Combinatorial Synthesis of Magnesium Tin Nitride Semiconductors. *J. Am. Chem. Soc.* **2020**, *142*, 8421–8430. [CrossRef] [PubMed]

202. Sun, W.; Bartel, C.J.; Arca, E.; Bauers, S.R.; Matthews, B.; Orvañanos, B.; Chen, B.R.; Toney, M.F.; Schelhas, L.T.; Tumas, W.; et al. A Map of the Inorganic Ternary Metal Nitrides. *Nat. Mater.* **2019**, *18*, 732–739. [CrossRef] [PubMed]

203. Choi, J.W.; Shin, B.; Gorai, P.; Hoye, R.L.Z.; Palgrave, R. Emerging Earth-Abundant Solar Absorbers. *ACS Energy Lett.* **2022**, *7*, 1553–1557. [CrossRef]

204. Javaid, K.; Wu, W.; Wang, J.; Fang, J.; Zhang, H.; Gao, J.; Zhuge, F.; Liang, L.; Cao, H. Band Offset Engineering in ZnSnN$_2$-Based Heterojunction for Low-Cost Solar Cells. *ACS Photonics* **2018**, *5*, 2094–2099. [CrossRef]

205. Lei, H.; Chen, J.; Tan, Z.; Fang, G. Review of Recent Progress in Antimony Chalcogenide-Based Solar Cells: Materials and Devices. *Sol. RRL* **2019**, *3*, 1900026. [CrossRef]

206. Akshay, V.V.; Benny, S.; Bhat, S.V. Solution-Processed Antimony Chalcogenides Based Thin Film Solar Cells: A Brief Overview of Recent Developments. *Sol. Energy* **2022**, *241*, 728–737. [CrossRef]

207. Ríos-Ramirez, B.; Nair, P.K. On the Stability of Operation of Antimony Sulfide Selenide Thin Film Solar Cells under Solar Radiation. *Phys. Status Solidi Appl. Mater. Sci.* **2018**, *215*, 1800479. [CrossRef]

208. Zakutayev, A.; Major, J.D.; Hao, X.; Walsh, A.; Tang, J.; Todorov, T.K.; Wong, L.H.; Saucedo, E. Emerging Inorganic Solar Cell Efficiency Tables (Version 2). *J. Phys. Energy* **2021**, *3*, 032003. [CrossRef]

209. Chen, C.; Tang, J. Open-Circuit Voltage Loss of Antimony Chalcogenide Solar Cells: Status, Origin, and Possible Solutions. *ACS Energy Lett.* **2020**, *5*, 2294–2304. [CrossRef]

210. Dong, J.; Liu, Y.; Wang, Z.; Zhang, Y. Boosting VOC of Antimony Chalcogenide Solar Cells: A Review on Interfaces and Defects. *Nano Sel.* **2021**, *2*, 1818–1848. [CrossRef]

211. Kojima, A.; Teshima, K.; Shirai, Y.; Miyasaka, T. Organometal Halide Perovskites as Visible-Light Sensitizers for Photovoltaic Cells. *J. Am. Chem. Soc.* **2009**, *131*, 6050–6051. [CrossRef]

212. Tien, C.H.; Lai, H.Y.; Chen, L.C. Methylammonium Halide Salt Interfacial Modification of Perovskite Quantum Dots/Triple-Cation Perovskites Enable Efficient Solar Cells. *Sci. Rep.* **2023**, *13*, 5387. [CrossRef]

213. Dey, A.; Ye, J.; De, A.; Debroye, E.; Ha, S.K.; Bladt, E.; Kshirsagar, A.S.; Wang, Z.; Yin, J.; Wang, Y.; et al. State of the Art and Prospects for Halide Perovskite Nanocrystals. *ACS Nano* **2021**, *15*, 10775–10981. [CrossRef]

214. Feng, B.; Duan, J.; Tao, L.; Zhang, J.; Wang, H. Enhanced Performance in Perovskite Solar Cells via Bromide Ion Substitution and Ethanol Treatment. *Appl. Surf. Sci.* **2018**, *430*, 603–612. [CrossRef]

215. Niu, T.; Lu, J.; Tang, M.-C.; Barrit, D.; Smilgies, D.-M.; Yang, Z.; Li, J.; Fan, Y.; Luo, T.; McCulloch, I.; et al. High Performance Ambient-Air-Stable FAPbI$_3$ Perovskite Solar Cells with Molecule-Passivated Ruddlesden–Popper/3D Heterostructured Film. *Energy Environ. Sci.* **2018**, *11*, 3358–3366. [CrossRef]

216. Jeong, J.; Kim, M.; Seo, J.; Lu, H.; Ahlawat, P.; Mishra, A.; Yang, Y.; Hope, M.A.; Eickemeyer, F.T.; Kim, M.; et al. Pseudo-Halide Anion Engineering for α-FAPbI3 Perovskite Solar Cells. *Nature* **2021**, *592*, 381–385. [CrossRef]

217. Hossain, M.K.; Toki, G.F.I.; Kuddus, A.; Rubel, M.H.K.; Hossain, M.M.; Bencherif, H.; Rahman, M.F.; Islam, M.R.; Mushtaq, M. An Extensive Study on Multiple ETL and HTL Layers to Design and Simulation of High-Performance Lead-Free CsSnCl$_3$-Based Perovskite Solar Cells. *Sci. Rep.* **2023**, *13*, 2521. [CrossRef]

218. Juarez-Perez, E.J.; Wußler, M.; Fabregat-Santiago, F.; Lakus-Wollny, K.; Mankel, E.; Mayer, T.; Jaegermann, W.; Mora-Sero, I. Role of the Selective Contacts in the Performance of Lead Halide Perovskite Solar Cells. *J. Phys. Chem. Lett.* **2014**, *5*, 680–685. [CrossRef]

219. Li, F.; Zhou, S.; Yuan, J.; Qin, C.; Yang, Y.; Shi, J.; Ling, X.; Li, Y.; Ma, W. Perovskite Quantum Dot Solar Cells with 15.6% Efficiency and Improved Stability Enabled by an α-CsPbI$_3$/FAPbI$_3$ Bilayer Structure. *ACS Energy Lett.* **2019**, *4*, 2571–2578. [CrossRef]

220. Yao, D.; Zhang, C.; Pham, N.D.; Zhang, Y.; Tiong, V.T.; Du, A.; Shen, Q.; Wilson, G.J.; Wang, H. Hindered Formation of Photoinactive δ-FAPbI3 Phase and Hysteresis-Free Mixed-Cation Planar Heterojunction Perovskite Solar Cells with Enhanced Efficiency via Potassium Incorporation. *J. Phys. Chem. Lett.* **2018**, *9*, 2113–2120. [CrossRef] [PubMed]

221. Xue, J.; Lee, J.-W.; Dai, Z.; Wang, R.; Nuryyeva, S.; Liao, M.E.; Chang, S.-Y.; Meng, L.; Meng, D.; Sun, P.; et al. Surface Ligand Management for Stable FAPbI$_3$ Perovskite Quantum Dot Solar Cells. *Joule* **2018**, *2*, 1866–1878. [CrossRef]

222. Sha, W.E.I.; Ren, X.; Chen, L.; Choy, W.C.H. The Efficiency Limit of CH$_3$NH$_3$PbI$_3$ Perovskite Solar Cells. *Appl. Phys. Lett.* **2015**, *106*, 221104. [CrossRef]

223. Masi, S.; Gualdrón-Reyes, A.F.; Mora-Seró, I. Stabilization of Black Perovskite Phase in FAPbI$_3$ and CsPbI$_3$. *ACS Energy Lett.* **2020**, *5*, 1974–1985. [CrossRef]

224. Zhang, H.; Li, Y.; Tan, S.; Chen, Z.; Song, K.; Huang, S.; Shi, J.; Luo, Y.; Li, D.; Meng, Q. High-Efficiency (>20%) Planar Carbon-Based Perovskite Solar Cells through Device Configuration Engineering. *J. Colloid Interface Sci.* **2022**, *608*, 3151–3158. [CrossRef] [PubMed]

225. Kim, M.; Kim, G.H.; Lee, T.K.; Choi, I.W.; Choi, H.W.; Jo, Y.; Yoon, Y.J.; Kim, J.W.; Lee, J.; Huh, D.; et al. Methylammonium Chloride Induces Intermediate Phase Stabilization for Efficient Perovskite Solar Cells. *Joule* **2019**, *3*, 2179–2192. [CrossRef]

226. Yin, J.; Xu, Z.; Hu, Q.; Teobaldi, G.; Liu, L.-M.; Prezhdo, O.V. Tuning Octahedral Tilting by Doping to Prevent Detrimental Phase Transition and Extend Carrier Lifetime in Organometallic Perovskites. *J. Am. Chem. Soc.* **2023**, *145*, 5393–5399. [CrossRef]

227. Wang, A.; Wang, J.; Niu, X.; Zuo, C.; Hao, F.; Ding, L. Inhibiting Octahedral Tilting for Stable CsPbI$_2$Br Solar Cells. *InfoMat* **2022**, *4*, 2–9. [CrossRef]

228. Menahem, M.; Dai, Z.; Aharon, S.; Sharma, R.; Asher, M.; Diskin-Posner, Y.; Korobko, R.; Rappe, A.M.; Yaffe, O. Strongly Anharmonic Octahedral Tilting in Two-Dimensional Hybrid Halide Perovskites. *ACS Nano* **2021**, *15*, 10153–10162. [CrossRef]

229. Lee, J.-H.; Bristowe, N.C.; Ho Lee, J.; Lee, S.-H.; Bristowe, P.D.; Cheetham, A.K.; Myung Jang, H. Resolving the Physical Origin of Octahedral Tilting in Halide Perovskites. *Chem. Mater.* **2016**, *28*, 4259–4266. [CrossRef]

230. Kim, G.; Min, H.; Lee, K.S.; Lee, D.Y.; Yoon, S.M.; Seok, S.I. Impact of Strain Relaxation on Performance of A-Formamidinium Lead Iodide Perovskite Solar Cells. *Science* **2020**, *370*, 108–112. [CrossRef]

231. Zhao, Q.; Hazarika, A.; Schelhas, L.T.; Liu, J.; Gaulding, E.A.; Li, G.; Zhang, M.; Toney, M.F.; Sercel, P.C.; Luther, J.M. Size-Dependent Lattice Structure and Confinement Properties in CsPbI$_3$ Perovskite Nanocrystals: Negative Surface Energy for Stabilization. *ACS Energy Lett.* **2019**, *5*, 238–247. [CrossRef]

232. Doherty, T.A.S.; Nagane, S.; Kubicki, D.J.; Jung, Y.K.; Johnstone, D.N.; Iqbal, A.N.; Guo, D.; Frohna, K.; Danaie, M.; Tennyson, E.M.; et al. Stabilized Tilted-Octahedra Halide Perovskites Inhibit Local Formation of Performance-Limiting Phases. *Science* **2021**, *374*, 1598–1605. [CrossRef] [PubMed]

233. Wang, R.; Xue, J.; Meng, L.; Lee, J.W.; Zhao, Z.; Sun, P.; Cai, L.; Huang, T.; Wang, Z.; Wang, Z.K.; et al. Caffeine Improves the Performance and Thermal Stability of Perovskite Solar Cells. *Joule* **2019**, *3*, 1464–1477. [CrossRef]

234. Wang, R.; Xue, J.; Wang, K.L.; Wang, Z.K.; Luo, Y.; Fenning, D.; Xu, G.; Nuryyeva, S.; Huang, T.; Zhao, Y.; et al. Constructive Molecular Configurations for Surface-Defect Passivation of Perovskite Photovoltaics. *Science* **2019**, *366*, 1509–1513. [CrossRef] [PubMed]

235. Xie, H.; Wang, Z.; Chen, Z.; Pereyra, C.; Pols, M.; Gałkowski, K.; Anaya, M.; Fu, S.; Jia, X.; Tang, P.; et al. Decoupling the Effects of Defects on Efficiency and Stability through Phosphonates in Stable Halide Perovskite Solar Cells. *Joule* **2021**, *5*, 1246–1266. [CrossRef]

236. Feng, W.; Tan, Y.; Yang, M.; Jiang, Y.; Lei, B.X.; Wang, L.; Wu, W.Q. Small Amines Bring Big Benefits to Perovskite-Based Solar Cells and Light-Emitting Diodes. *Chem* **2022**, *8*, 351–383. [CrossRef]

237. Yang, T.; Gao, L.; Lu, J.; Ma, C.; Du, Y.; Wang, P.; Ding, Z.; Wang, S.; Xu, P.; Liu, D.; et al. One-Stone-for-Two-Birds Strategy to Attain beyond 25% Perovskite Solar Cells. *Nat. Commun.* **2023**, *14*, 839. [CrossRef]

238. Li, G.; Song, J.; Wu, J.; Song, Z.; Wang, X.; Sun, W.; Fan, L.; Lin, J.; Huang, M.; Lan, Z.; et al. Efficient and STable 2D@3D/2D Perovskite Solar Cells Based on Dual Optimization of Grain Boundary and Interface. *ACS Energy Lett.* **2021**, *6*, 3614–3623. [CrossRef]

239. Campos, T.; Dally, P.; Gbegnon, S.; Blaizot, A.; Trippé-Allard, G.; Provost, M.; Bouttemy, M.; Duchatelet, A.; Garrot, D.; Rousset, J.; et al. Unraveling the Formation Mechanism of the 2D/3D Perovskite Heterostructure for Perovskite Solar Cells Using Multi-Method Characterization. *J. Phys. Chem. C* **2022**, *126*, 13527–13538. [CrossRef]

240. Weidman, M.C.; Seitz, M.; Stranks, S.D.; Tisdale, W.A. Highly Tunable Colloidal Perovskite Nanoplatelets through Variable Cation, Metal, and Halide Composition. *ACS Nano* **2016**, *10*, 7830–7839. [CrossRef]

241. Zhou, T.; Lai, H.; Liu, T.; Lu, D.; Wan, X.; Zhang, X.; Liu, Y.; Chen, Y. Highly Efficient and Stable Solar Cells Based on Crystalline Oriented 2D/3D Hybrid Perovskite. *Adv. Mater.* **2019**, *31*, e1901242. [CrossRef] [PubMed]

242. Sutanto, A.A.; Caprioglio, P.; Drigo, N.; Hofstetter, Y.J.; Garcia-Benito, I.; Queloz, V.I.E.; Neher, D.; Nazeeruddin, M.K.; Stolterfoht, M.; Vaynzof, Y.; et al. 2D/3D Perovskite Engineering Eliminates Interfacial Recombination Losses in Hybrid Perovskite Solar Cells. *Chem* **2021**, *7*, 1903–1916. [CrossRef]

243. Cho, Y.; Soufiani, A.M.; Yun, J.S.; Kim, J.; Lee, D.S.; Seidel, J.; Deng, X.; Green, M.A.; Huang, S.; Ho-Baillie, A.W.Y. Mixed 3D–2D Passivation Treatment for Mixed-Cation Lead Mixed-Halide Perovskite Solar Cells for Higher Efficiency and Better Stability. *Adv. Energy Mater.* **2018**, *8*, 1703392. [CrossRef]

244. Al-Ashouri, A.; Köhnen, E.; Li, B.; Magomedov, A.; Hempel, H.; Caprioglio, P.; Márquez, J.A.; Vilches, A.B.M.; Kasparavicius, E.; Smith, J.A.; et al. Monolithic Perovskite/Silicon Tandem Solar Cell with >29% Efficiency by Enhanced Hole Extraction. *Science* **2020**, *370*, 1300–1309. [CrossRef] [PubMed]

245. Wang, J.; Uddin, M.A.; Chen, B.; Ying, X.; Ni, Z.; Zhou, Y.; Li, M.; Wang, M.; Yu, Z.; Huang, J. Enhancing Photostability of Sn-Pb Perovskite Solar Cells by an Alkylammonium Pseudo-Halogen Additive. *Adv. Energy Mater.* **2023**, *13*, 2204115. [CrossRef]

246. Ren, M.; Qian, X.; Chen, Y.; Wang, T.; Zhao, Y. Potential Lead Toxicity and Leakage Issues on Lead Halide Perovskite Photovoltaics. *J. Hazard. Mater.* **2022**, *426*, 127848. [CrossRef]

247. Torrence, C.E.; Libby, C.S.; Nie, W.; Stein, J.S. Environmental and Health Risks of Perovskite Solar Modules: Case for Better Test Standards and Risk Mitigation Solutions. *iScience* **2023**, *26*, 105807. [CrossRef] [PubMed]

248. Aftab, A.; Ahmad, M.I. A Review of Stability and Progress in Tin Halide Perovskite Solar Cell. *Sol. Energy* **2021**, *216*, 26–47. [CrossRef]

249. Mahmoudi, T.; Rho, W.Y.; Kohan, M.; Im, Y.H.; Mathur, S.; Hahn, Y.B. Suppression of Sn^{2+}/Sn^{4+} Oxidation in Tin-Based Perovskite Solar Cells with Graphene-Tin Quantum Dots Composites in Active Layer. *Nano Energy* **2021**, *90*, 106495. [CrossRef]

250. Chen, Z.; Liu, M.; Li, Z.; Shi, T.; Yang, Y.; Yip, H.L.; Cao, Y. Stable Sn/Pb-Based Perovskite Solar Cells with a Coherent 2D/3D Interface. *iScience* **2018**, *9*, 337–346. [CrossRef]

251. Ban, H.; Sun, Q.; Zhang, T.; Li, H.; Shen, Y.; Wang, M. Stabilization of Inorganic $CsPb_{0.5}Sn_{0.5}I_2Br$ Perovskite Compounds by Antioxidant Tea Polyphenol. *Sol. RRL* **2020**, *4*, 1900457. [CrossRef]

252. Li, C.; Pan, Y.; Hu, J.; Qiu, S.; Zhang, C.; Yang, Y.; Chen, S.; Liu, X.; Brabec, C.J.; Khaja Nazeeruddin, M.; et al. Vertically Aligned 2D/3D Pb–Sn Perovskites with Enhanced Charge Extraction and Suppressed Phase Segregation for Efficient Printable Solar Cells. *ACS Energy Lett.* **2020**, *5*, 1386–1395. [CrossRef]

253. Zhou, X.; Zhang, L.; Wang, X.; Liu, C.; Chen, S.; Zhang, M.; Li, X.; Yi, W.; Xu, B. Highly Efficient and Stable GABr-Modified Ideal-Bandgap (1.35 EV) Sn/Pb Perovskite Solar Cells Achieve 20.63% Efficiency with a Record Small Voc Deficit of 0.33 V. *Adv. Mater.* **2020**, *32*, e1908107. [CrossRef]

254. Sanchez-Diaz, J.; Sánchez, R.S.; Masi, S.; Krečmarová, M.; Alvarez, A.O.; Barea, E.M.; Rodriguez-Romero, J.; Chirvony, V.S.; Sánchez-Royo, J.F.; Martinez-Pastor, J.P.; et al. Tin Perovskite Solar Cells with >1300 h of Operational Stability in N_2 through a Synergistic Chemical Engineering Approach. *Joule* **2022**, *6*, 861–883. [CrossRef] [PubMed]

255. Zhu, Z.; Jiang, X.; Yu, D.; Yu, N.; Ning, Z.; Mi, Q. Smooth and Compact $FASnI_3$ Films for Lead-Free Perovskite Solar Cells with over 14% Efficiency. *ACS Energy Lett.* **2022**, *7*, 2079–2083. [CrossRef]

256. Yu, B.B.; Chen, Z.; Zhu, Y.; Wang, Y.; Han, B.; Chen, G.; Zhang, X.; Du, Z.; He, Z. Heterogeneous 2D/3D Tin-Halides Perovskite Solar Cells with Certified Conversion Efficiency Breaking 14%. *Adv. Mater.* **2021**, *33*, e2102055. [CrossRef] [PubMed]